Ruben Vilnes Iden

Design of Superconducting Propulsion Motor for Hydrogen-Powered Zero-Emission Aviation

Master's thesis

NTNU
Norwegian University of
Science and Technology

Ruben Vilnes Iden

Design of Superconducting Propulsion Motor for Hydrogen-Powered Zero-Emission Aviation

Master's thesis in Energi og Miljø
Supervisor: Jonas Kristiansen Nøland
Co-supervisor: Runar Mellerud
June 2023

Norwegian University of Science and Technology
Faculty of Information Technology and Electrical Engineering
Department of Electric Power Engineering

NTNU
Norwegian University of
Science and Technology

Sammendrag

Dette master prosjektet presenterer et ferdigstilt design av en mega-watt skalert superledende slotless PMSM for luftfartsapplikasjoner. Ved bruk av elektromagnetisk analyse i COMSOL ble optimale geometriske parametere dedusert. I slotless maskiner spiller størrelse på spolen og avstanden mellom de en betydelig rolle i effekttetthet, der større rekkevidde langs omkretsen fører til en mer effektiv utnyttelse av strømen indusert i spolen. Overraskende førte økning av luftgapradiusen til redusert momentproduksjon, som er motsetning til teoretiske forventninger. Derfor førte mindre luftgapradius til bedre effekttettheten. Viklingskonfigurasjoner med høyere antall spoler presterte generelt sett bedre enn de med færre spoler. Implementering av en Halbach-array reduserte vekten ved å eliminere rotorjernet. Innføringen av TA-formuleringen ga tilgang til AC-tap i superlederene. Ytelsen til superlederne ble sterkt påvirket av flukstetthetsfeltet i luftgapet. Områder nærmest magnetene opplevde lavere kritisk strømtetthet, noe som førte til økte tap. Sidene på de superledende båndene viste den høyeste strømtettheten. Driftstemperatur og strømbelastning spilte en viktig rolle i tapsgenereringen. Ved å sette strømbelastningen til 20% og driftstemperaturen til 60 K, ble akseptable tapsnivåer oppnådd ved 78 W i gjennomsnitt over en periode for hver spole. Den designede motoren oppnådde en krafttetthet på 24,7 kW/kg, som overgår industriens mål på 20 kW/kg. Disse resultatene viser at mulighetene for å integrere superledere i luftfartsapplikasjoner er lovende, men videre analyse er nødvendig med tanke på hvor mange faktorer som ikke ble tatt høyde for i denne studien.

Design of Superconducting Propulsion Motor for Hydrogen-Powered Zero-Emission Aviation

Ruben Vilnes Iden

Department of Electric Power Engineering

Norwegian University of Science and Technology

Supervisor: Jonas Kristiansen Nøland (NTNU)

CO-supervisor: Runar Mellerud (NTNU)

Abstract—This master project presents a design of a mega-watt scaled superconducting slotless PMSM for aviation applications. The process was divided into two parts in the FEM software, COMSOL: an electromagnetic analysis, and a study of the superconductors with TA formulation. The first investigation yielded the geometrical parameters for the machine. Given its significant impact on machine performance for application in the aviation industry, the power density was determined to be the parameter of the most significance. The research discovered the great importance of coil size and coil placement. Lower torque production occurred when the coils did not cover enough of the air gap circumference. This phenomenon meant a shorter air gap radius resulted in better power density for the machine, when the coil size was maintained the same. A preliminary winding layout study concluded that a 24-slot and 8-pole winding design gave an excellent performance for this topology and power ratings. The implementation of the TA formulation yielded access to the AC losses in the superconductors. It demonstrated that the magnetic flux density in the air gap greatly affected the critical current density. The region closest to the magnets contained the lowest values. This phenomenon was primarily due to the exposure of the coils due to the lack of stator slots. The temperature and current loading of the superconductor significantly affected the losses. Setting them to a reasonable value yielded acceptable losses in superconductors. Temperature of 60K and current loading of 20% yielded 78W average SC losses over an electrical period for one coil. Ultimately, the studies resulted in a machine producing 1.52MW weighing only 70kg, with the rotational speed of 3500 rpm. Power density of 24,7kg/kW shows excellent promise from this design, but further analysis needs to be conducted given the number of factors neglected in this study.

Index Terms—PMSM, slotless, superconductor, HTS, TA formulation, Aviation, AC losses, REBCO

I. INTRODUCTION

Annually the air industry is projected to grow worldwide by 5 percent; this gives great motivation to improve the industry's efficiency. Today's technology gives high emissions and noise with the use of jet engines for aircraft propulsion. The recent improvement in technology and materials used for electrical machines have made them realistic options for replacing today's jet-fueled aircraft. The ACARE (Advisory Council for aviation research and innovation in Europe) has created a flight path for 2050, which targets goals of environmental-impact reduction related to the numbers from 2000. See table I. These sets targets of both emissions- and

TABLE I
SUMMARY OF THE ACARE FLIGHT-PATH 2050 GOALS [2]

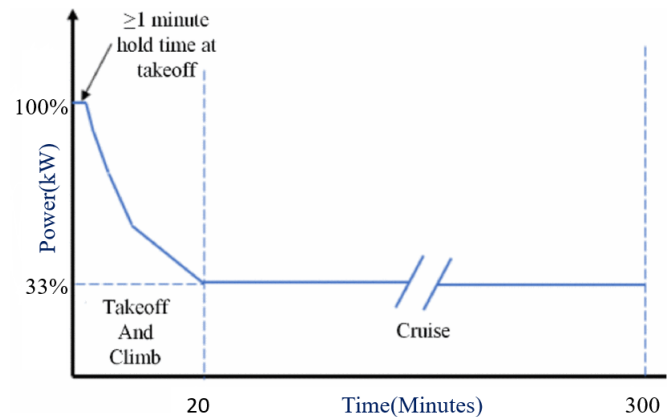| Environmental factor	EU ACARE fligthpath 2050 strategy
Greenhouse gas emissions (GHB)	75 CO_2 emission reduction
Nitrogen oxides NOx	90% NOx reduction
Noise	65% reduction in noise
Safety	80% reduction in accidents compared to the year 2000

Fig. 1. ASCEND, requirement for mechanical power as a function of time flight profile. [3]

noise-reducing configurations.

With the implementation of electrical machines, more problems arise than with Jet fuel engines, especially weight, and reliability problems [1]. Historically, electrical machines have been heavy and unreliable compared to today's jet engines, making them unfeasible. These combined are the challenging design factors that will determine the usability of the future propulsion system in the aviation industry.

An important design factor will be the power density of the motor; each kilogram added to the application weakens the design. Unfortunately, today's electrical motors are not designed for such high power density as set for the aviation industry. Generally, they are power-dense-restricted due to the copper winding and torque production. Current

2

technologies produce machines with 1-5 kW/kg power densities. Current research targets power density up to 20 KW/kg [4].

An incremental factor for all electric motors used in applications is the reliability of the whole system, but even more for aircraft applications where faults can cause fatal consequences. Therefore fault tolerance for the whole drive system is some of the main considerations normally done in the design process [5]. An advantage for aircraft is that the run profile is entirely predictable and requires maximum power only from the takeoff. So if a fault should occur in the machine after the takeoff, the aircraft can still be able to finish the run [3]. The efficiency of the machine greatly determines the performance parameters. High-efficiency motors require less fuel for the drive, and given the importance of weight for the whole application, efficient motors will be weight-saving. In addition, to meet the targets for reduction in emissions, high efficiency will help the industry reach its sustainability targets [2].

In order to meet the demands proposed by the industry, many researchers investigate the possibility of using superconducting(SC) machines for the aviation industry [7], [8], [9]. With the recent advancement in material technology regarding superconductors, the rise of interest in high-temperature superconducting(HTS) machines has appeared the recent years [10]. The potential for extreme current densities makes SC and especially HTS a very viable alternative to the traditional litz wire [11]. But with the implementation of SC, new design problems arise. Such as AC losses, quenching, and cooling [12].

The slotless machine is a type of electric machine that does not have the traditional slots found in conventional electric machines. By eliminating slots, the machine can operate at higher speeds with lower losses and higher power densities [13]. This makes slotless machines a suitable candidate for high-performance applications in the aviation industry.

This study aims to design and analyze a slotless PMSM that meets the performance requirements for aviation industry applications. More specifically, the power ratings of the machine presented in this paper [4]. An analytical model will be developed and then implemented in Comsol to achieve this goal, done in section III. This model will serve as the basis for the optimization process. The optimization

process will determine the electrical and geometrical parameters of the machine, section IV. Given its significant impact on machine performance in the aviation industry, the focus will primarily be on the power density parameter. Additionally, the study will consider how implementing superconductors affects machine performance. The TA formulation will be utilized to estimate the AC losses in the superconducting material. With these simulations, a better understanding of the behavior of the machine at different operating temperatures will be obtained, section V. Further considerations of geometrical and electrical parameters will be done based on these results before a finished model is presented in the last section, section VI. Here the most relevant machine parameters will be given.

From my specialization project leading up to the master project, research about a similar topic was conducted. Thus some of the material from this project have been adapted into the master project. The sections I and III have been based upon similar sections in the specialization project. In section II, the subsection about HTS and cryo-cooling was adapted and improved from the specialization project.

II. THEORY

In this section relevant theory will be presented in order to support the analysis and discussion conducted in this project.

A. High-temperature superconductor and cryo-cooling

Superconductors are materials that can operate in a superconducting state, that gives the material zero electrical resistance. Superconductors can be divided into low-temperature(LTS) and high-temperature superconductors. However, HTS is usually the only type considered for high-performance applications. The definition of HTS states that the critical temperature is to be above 77K. SC can also be divided into type-I, and type-II, where type-I are pure metals and type-II are alloys and complex oxides of ceramics. Generally, type-II is preferred, given the ability to operate in all three conductivity states [14].

1) Critical values: Conductors can exist in three states: normal, mixed, and Meissner. In the Meissner state, a conductor becomes superconducting and exhibits perfect diamagnetism, repelling all external magnetic fields and lacking any internal magnetic field. The mixed state occurs when the applied magnetic field exceeds a threshold called H_{c1}, as illustrated in figure 2. In this state, the superconductor develops regions with incomplete superconducting abilities, known as vortices, where magnetic flux penetrates the material. As the magnetic field strength increases, the number of vortices grows, reducing the superconducting area. Eventually, when the magnetic field reaches the upper critical field limit, H_{c2}, the superconducting region disappears completely, and the material returns to its normal state, see figure 2.

The ability of superconductivity relies on three critical parameters, temperature, magnetic field, and current density,
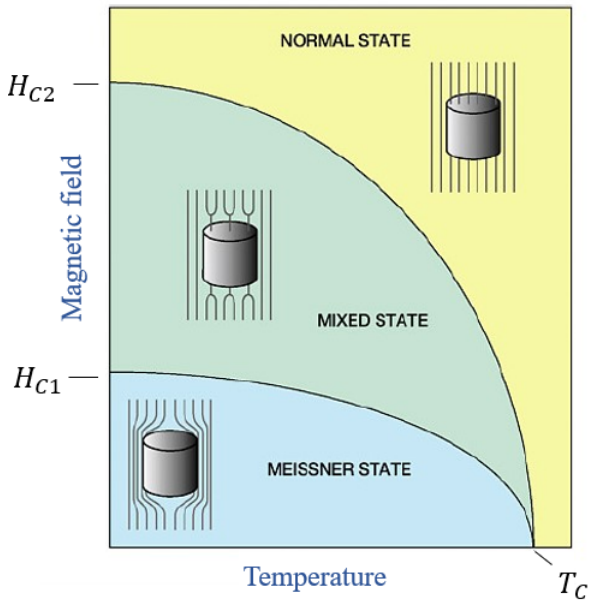
Fig. 2. Conducting states dependent on temperature and applied magnetic field, only type-II SC can operate in all three states states [15]. H_{C1} and H_{C2} are the critical magnetic fields, while T_c is the critical temperature.
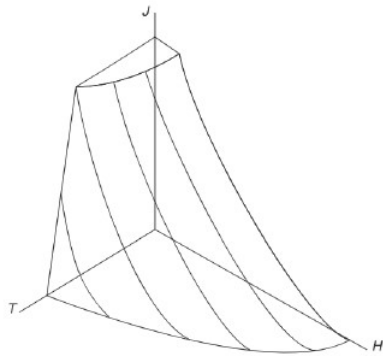

Fig. 3. Critical values, J_c, H_c and H_c. The area inside demonstrates the superconducting operating area. [17]

all of which must remain below their respective critical limits: T_c, H_c, and J_c. When a current flows through a material, a magnetic field forms around it. If this self-generated magnetic field, combined with the applied magnetic field, exceeds the critical value H_c at the conductor's surface, the material transitions out of the mixed state. This transition occurs at a critical current, I_c, which depends on the temperature and the applied magnetic field [16]. Therefore, the critical values for superconductivity are interconnected and restrict each other's ranges, as depicted in figure 3.

2) AC losses: Superconductors exhibit negligible losses in DC conditions. However, losses can occur when exposed to alternating current. Generally, they are significantly lower than those in conventional conductors with similar current ratings. These losses, known as "AC losses" or "cold losses," can be categorized into magnetization losses and transport

current losses [18]. Magnetization losses are divided into three branches hysteresis, coupling, and eddy current losses. While transport current losses divide into hysteresis losses and flux flow current losses [18]. In designing a superconducting machine, it is crucial to investigate eddy current losses as they hold the most significance. When a superconductor is exposed to a varying magnetic field over time, eddy currents are induced within the conductor. The angle of the interaction between the applied magnetic field and the conductor holds importance, especially for SC manufactured as thin strips. If the magnetic field interacts on the side of the strip, less eddy current will occur compared to interacting normally on the strips, given the small surface area on the side compared to the top. In addition, eddy current losses increase proportionally with the square of the frequency f^2, causing them to be more detrimental at higher frequencies.
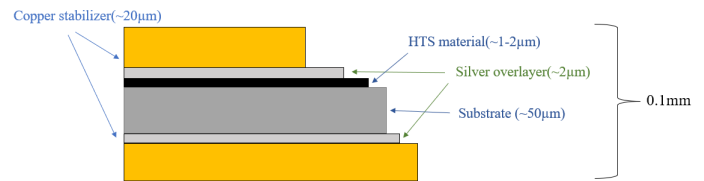

Fig. 4. A simple visualization of a REBCO superconductor tape, consists of different layers where only the inner part consists of HTS material. The heights are example height for a potential tape. The figure dimensions are not to scale.

3) Cryo-cooling: Cooling at cryogenic temperatures is considered "expensive," given the cooling penalty and higher demands for insulation. This is normally called "cold losses" [19]. The cooling penalty is the increased energy needed to remove losses at low temperatures [18]. This phenomenon makes even small losses a potential problem.
Given the operational temperature of the HTS, the need for cryo-cooling has reduced the feasibility and interest in HTS technology for airplane machines due to the weight and cost of cryo-coolers [20]. However, with the use of liquid hydrogen as fuel, implementing HTS machines seems more feasible since the fuel works both as an energy source and a cryogenic cooler. The liquid hydrogen needs to be heated up to the temperature of the gas state before entering the electricity-producing fuel cells. With this synergy, the cooling can be seen as "free." This design increases the limits for acceptable AC losses because of the plentiful coolant supply. The idea is presented in [21].

4) Quenching: HTS allows extreme temperature and current density conditions, making the system quite fragile to faults. Therefore, quenching could cause detrimental faults. Quenching is when the SC suddenly loses superconductivity because one of the critical factors is exceeded. This leads to higher losses due to the now-added resistive losses, which are extremely high relative to the AC losses before

4

quenching [22]. In most cases this makes the conductors burn up when quenching is achieved.

5) REBCO superconductors: Rare Earth Barium Copper Oxide (REBCO) superconductors are a class of high-temperature superconductors (HTS) that have obtained significant attention in recent years due to their potential for use in a variety of applications [23]. REBCO superconductors combine rare earth elements, such as yttrium and neodymium, with barium, copper, and oxygen in different layers, see figure 4. REBCO SCs are produced as thin strip tapes with a high width-to-height ratio. The superconducting layer is only 1μm, while the whole tape is generally around 0.1mm. REBCO has a higher critical temperature than many other HTS materials. In addition, they have a higher critical current density [24], which is the maximum amount of current that can be carried without losing superconductive ability. This feature makes them particularly attractive for high-power applications such as motors, generators, and transmission lines. The development of REBCO superconductors has been motivated by the need to improve the efficiency of electrical power systems. Despite their potential advantages, the development of REBCO superconductors has been challenging due to the difficulty of synthesizing high-quality REBCO materials with desirable properties [16]. Researchers are also working to overcome other technical challenges, such as improving the stability and durability of REBCO superconductors in practical applications. Despite these challenges, REBCO superconductors hold great promise for a wide range of technological applications, and research in this area will likely continue to advance in the coming years.

B. TA-formulation

TA formulation is a theoretical framework to model superconductor losses. In the superconducting state, the material conducts with zero resistance. However, AC losses occur with alternating current due to the alternating fields acting on the conductors. TA formulation uses partially differential equations to model the current vector potential, allowing the formulation to calculate the AC losses accurately.

Earlier H formulation has been the most used method, given its ease of implementation in FEM software. But due to a large number of computational steps for the formulation, using more complicated models such as electrical machines yields long computational times [25]. The DOF(degrees of freedom) are quite high in thin tapes. So in recent years, the T-A formulation has proved to be a competitive alternative for modeling systems with a large number of HTS conductors, where the superconducting layer is regarded as an infinitely thin sheet, and the variation of the electromagnetic quantities across its thickness can be neglected [26].

The TA formulation is divided into two different formulations. T-formulation solves the current vector potential, $\vec{T}$, for the superconducting domain, while A-formulation solves the magnetic vector potential for the whole domain. The current density vector potential, $\vec{T}$, is solved using the Maxwell's equations, [1]-[3]:

$$\vec{J} = \nabla \times \vec{T} \tag{1}$$

$$\nabla \times \vec{E} = -\frac{\partial \vec{B}}{\partial t} \tag{2}$$

$$\vec{E} = \rho \vec{J} \tag{3}$$

Combining these three equations results in:

$$\nabla \times \rho \nabla \times \vec{T} = -\frac{\partial \vec{B}}{\partial t} \tag{4}$$

Equation 4 is the basis of the T-formulation. It is used to determine the change in flux density in the superconducting area using the current vector potential.

In order to simplify equation 4, certain assumptions and simplifications can be made. The analysis of the system is conducted in a Cartesian coordinate system, where $\vec{T}$ is zero in both the x-direction and z-direction. Additionally, the variation of vector $\vec{T}_y$ only occurs along the x-axis. The simplifications results in the following equations.

$$-\frac{\partial \vec{B}}{\partial t} = \begin{bmatrix} 0 \\ -\frac{\partial}{\partial x} \rho \frac{\partial}{\partial x} T_y \\ 0 \end{bmatrix} \tag{5}$$

Eq. 5 shows that the magnetic density field will only vary in the y-direction with a changing x. The formulation is now scaled down to scalar form. See figure 5.

1) Current: To apply a current to the SC, boundary conditions are applied. The current can be represented by an integral of the current density over the cross-section of the SC, this yields the transport current of the SC [26]. Furthermore, implementing Stokes' theorem gives.

$$I_{SC} = \iint_S \vec{J} dS = \iint_S \nabla \times \vec{T} dS = \oint_{dS} \vec{T} dr \tag{6}$$

Using eq. 7 and analyzing figure 6, and 5 , the expression can be simplified. T_1 and T_2 are the current vector potential at each side of the SC, as can be seen from figure 6.

$$I_{SC} = \oint_{dS} \vec{T} dr = (T_1 - T_2)\delta \tag{7}$$

δ, is the height of the superconducting layer, given by the material choice.

$$J_{sf} = T_1 - T_2 = \frac{I_{SC}}{\delta} \tag{8}$$

J_{sf} applied at the boundary results in the transport current for the SC material in the T formulation.
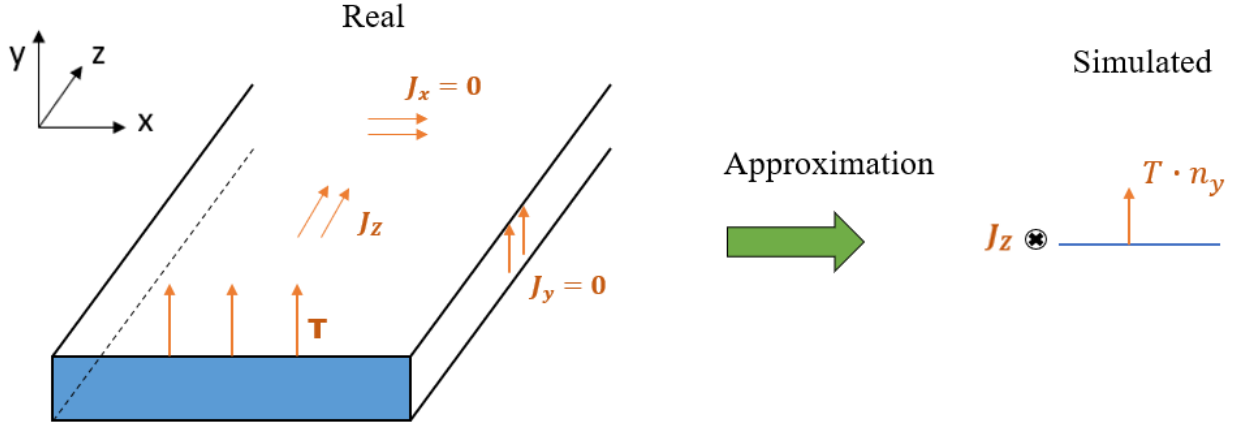
Fig. 5. Single HTS tape illustrated in 3D relative to the coordinate system and how the TA formulation transform the problem into a 1D-tape case.
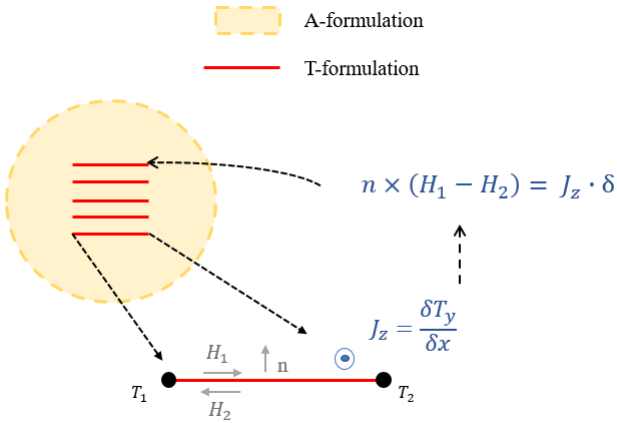

Fig. 6. This figure visualize the interaction between the T and A formulation. The current density in z-direction from the T formulation, J_z, is put into the A formulation as an external surface current on the boundaries between the formulations.

2) Coupling between T-domain and A-domain: The coupling of the two formulations begins with the current density calculated in the T-formulation and, after that, applied as an external surface current density on the side of the tape in the A formulation, see figure 6. With the following equation:

$$\vec{n} \times (\vec{H_1} - \vec{H_2}) = J_z \cdot \delta \qquad (9)$$

To determine the boundary condition in T-formulation of the top and bottom parallel to the tape, Neumanns condition is implemented:

$$\frac{\delta(T_x n_x + T_y n_y)}{\delta n} = 0 \qquad (10)$$

Simplification can be made, given that $\vec{T}$ is zero in the x-direction.

$$\frac{\delta T_y}{\delta y} = 0 \qquad (11)$$

3) Resistivity: In order to model the resistivity of the material, the E-J power law is used:

$$\rho_{SC} = \frac{E_c}{J_c(\mathbf{B})} \left| \frac{|J|}{J_c(\mathbf{B})} \right|^{N-1} \qquad (12)$$

Here the critical current density is calculated from a "Kim-like model". This model calculates the critical current density depending on the applied magnetic field and temperature. This yields a more accurate model, given the dependency on applied magnetic field for the critical current density in the SC material. The equation for the Kim-like model follows below [18]:

$$J_c(\mathbf{B}) = \frac{J_c(0)}{\left(1 + \frac{\sqrt{\frac{1}{\gamma}(B_{par}^2 + B_{perp}^2)}}{B_0}\right)^{\alpha}} \qquad (13)$$

Here $J_c(0)$ is the critical current density in self field, α, γ, and B_0 are constants that are determined from the material and operating temperature. This variation of Kims model has showed good results of replicating the experimental data [27].

C. Halbach array

The halbach array is permanent magnets divided into multiple segments per pole, where the segments for one pole are shifted rotational, as shown in figure 7. Using two or four segments is most common, with different benefits and disadvantages. Two segments per pole generate a trapezoidal flux density in the air gap, [28], while the four segments pole generates more of a sinusoidal flux density. The choice of the number of segments per pole depends on the specific application and the desired magnetic field distribution.

One of the Halbach array's most significant advantages is eliminating the rotor yoke in conventional permanent magnet synchronous motor(PMSM). In conventional designs, the permanent magnet is directed outwardly [29]. The flux needs a path from north to south. The path with the
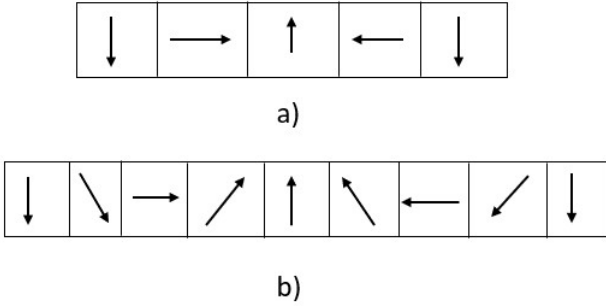
Fig. 7. Halbach array with two segments per pole (a) and four segments per pole (b).

lowest reluctance will be where the flux flows. Adding a rotor yoke solves this problem. However, the rotor yoke adds non-power contributing weight, which could be more beneficial to remove to save weight. The segmented magnets provide the low reluctance flux path for the rotor, removing the need for a rotor yoke and saving weight.

A negative effect is the risk of de-magnetization. If the magnet's flux density field gets below a specific value due to the opposing field from the coils, the flux density will not reach its initial remanent flux density, weakening the permanent magnet's future performance. This effect is particularly relevant in high-speed applications, where the magnetic field changes rapidly.

D. Slotless topology

In a slotless motor, the coils are placed between the rotor and stator, which eliminates the stator teeth and reduces the weight of the motor. Slotless topology allows for lower losses in the stator given the elimination of the teeth stator [13].

Another advantage of the slotless design is the reduction of cogging torque, which is caused by the interaction between the permanent magnets in the rotor and the stator teeth. Cogging is a common issue in slotted motor designs, and its effect can harm low-speed applications. With a slotless design, the cogging effect is limited, resulting in smoother torque in the air gap, [30]. Additionally, a slotless motor design provides greater freedom in dimensioning the motor since fewer restrictions are required, particularly in reducing the cogging torque.

However, there are challenges to consider with the slotless design, particularly regarding torque production. The air gap in a slotless design is typically longer than in a slotted design. This results in increased reluctance because air is a worse magnetic flux conductor. This results in lower air gap flux density, reducing torque production.

III. Preliminary design of slotless PM machine with superconducting coils

As a part of my specialization project, a typology study was conducted regarding HTS machines for high-speed mega-watt scale applications for the aviation industry, see Appendix B for data. SC implementation shows excellent promise for radial flux synchronous machines from the topology study. Slotless, slotted, and HTS rotor configurations are all being researched for implementation of SC. Configurations using HTS for rotors, such as HTS bulk and HTS wound, showed great potential, but they are still in an early phase regarding technology readiness level(TRL). The study, therefore, found the PMSM rotor configuration most promising in the near future for aviation applications. The slotless approach for the stator showed great potential for a high power density. Both inner and outer rotors were discussed for this approach, but due to more accessible cooling with the inner rotor approach, this was deemed more feasible for SC implementation. The axial flux machine comes with high torque and power density. However, the size of the discs is inherently limited by centrifugal forces. Few cases of axial flux machines met the power and speed requirements. Research with HTS in AFM is quite rare to be found as well. Therefore, this study concluded that slotless typology with an inner rotor is a promising approach for HTS aircraft applications.

Given the results of the topology study, a high-speed mega-watt slotless PMSM with SC in the stator coils was to be designed. To obtain starting values for the design, an analytical design process was conducted based on the performance ratings $P_{mech} = 2.5$MW and $n_{rpm} = 3500$rpm. After that, a finite element analysis was performed in COMSOL to evaluate the potential of this type of machine in comparison to a slotted PMSM [4].

A. Initial scaling: Bore volume

The design of a PMSM with superconductors in the stator coils involves several important considerations. One of the initial steps in the design process is the determination of the volume of the rotor and the corresponding air gap radius. The air gap radius plays a crucial role in the performance of the PMSM, as it significantly affects the torque production capability of the machine. This relationship is governed by the power input, speed, flux density, and air gap radius, as described by equation 14. Therefore, correctly selecting the air gap radius is essential to ensure that the PMSM operates at optimal performance levels, including efficiency and power density.

$$T_{em} = \frac{\pi}{4} D_r^2 l \hat{A} \hat{B}_\delta \, cos\zeta_r \qquad (14)$$

The most relevant parameters are T_{em}, electromagnetic torque, D_r, outer rotor diameter, and $\hat{A}$, linear current density. In addition, from pyrhonen [31], parameters for tangential stress tensor, air gap length, machine length, and diameter

7

ratio were found. Based on common industry assumptions for PMSM.

B. Stator yoke

The yoke design is an important consideration, as yoke losses are a prominent contributor to overall losses in electrical machines. The machine is assumed to be laminated, and the eddy current losses can be neglected. Leaving only the hysteresis losses to be considered. These losses depend on the magnetic flux density and the machine's operating speed. For a machine with a nominal operating speed of 3500 rpm, it is necessary to design the yoke to withstand the magnet flux density at operating conditions. The saturation of the steel in the yoke increase losses, so it is essential to consider the maximum allowed flux when designing the height of the yoke for the stator. Using materials with high magnetic saturation and low hysteresis losses can help minimize yoke losses in the machine.
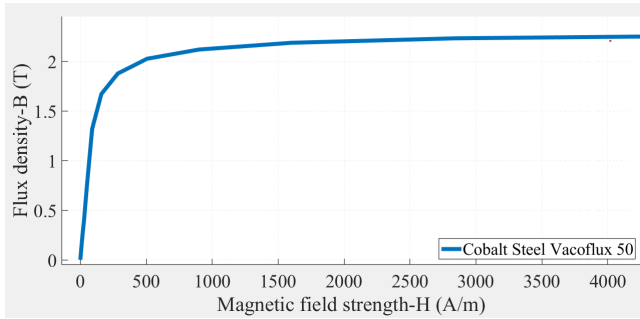

Fig. 8. BH-curve of Cobalt Steel Vacoflux 50, data collected from COMSOL.

$$\Phi_p = B_{s,peak} \cdot \tau_p \cdot l_r \cdot \alpha_i \tag{15}$$

$$h_{ys} = \frac{\Phi_p}{B_{ts} \cdot K_{ir} \cdot 2 \cdot l_r} \tag{16}$$

Here Φ_p is the flux generated in each pole, K_{ir} the lamination pack coefficient, h_{ys} the stator yoke height, and B_{ts} the stator maximum flux density. The maximum value can be found from the BH curve, where the material saturates; see figure 8. The maximum value for stator yoke flux density was set to 2.0T.

C. Magnets

To determine the height of the magnets, the approach from pyrhonen [31] was used to obtain a reasonable first value for the height. Pyrhonen assumes a PM(permanent magnet) configuration with one segment for each pole. Instead, a Halbach array was chosen with four segments per pole. More than four segments complicate the design and add extra expenses [32]. Therefore, four segments per pole were chosen. The rotor yoke can be removed with a Halbach array, saving weight
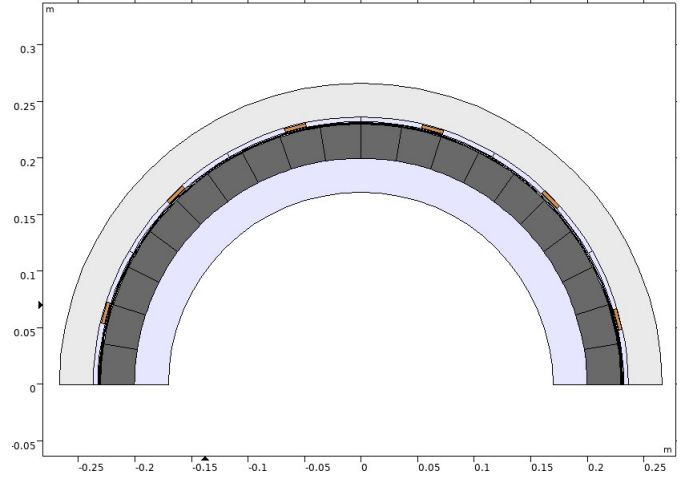

Fig. 9. Preliminary COMSOL model, half of the design is implemented given the periodicity of the slot and pole configuration.

Fig. 10. Winding layout with one layer, found from Emetor [33].

$$B_g = \frac{\pi}{4} \cdot \frac{1}{sin(\alpha_m \cdot \frac{\pi}{2})} \cdot B_{g1} \tag{17}$$

$$g_{eq} = g \cdot K_c \tag{18}$$

$$l_{eq} = \frac{-B_g \cdot g_{eq}}{B_g - B_r} \tag{19}$$

$$l_m = \frac{l_{eq}}{\mu_r} \tag{20}$$

g_{eq}, K_c, B_r, l_{eq} and l_m is the equivalent air gap length, Carter coefficient, remnant flux density, equivalent magnet length and actual magnet length. The height of the magnet should be able to create the desired air gap flux density. In Comsol, the magnet height was adjusted so that it was able to meet the requirements. As well as producing the correct air gap flux density, the magnets should be able to function as a flux path.

D. Winding layout

The software Emetor [33] was used to find an appropriate initial winding layout. 12 slots and 10 poles were used as a starting point, given that the slotted machine, [34], used the same layout. With 12 slots and 10 poles, one layered concentrated windings were the optimal choice. Given the layout, a periodicity of 2 was used to save computation time, with periodic condition set to anti-periodicity. See figure 10.
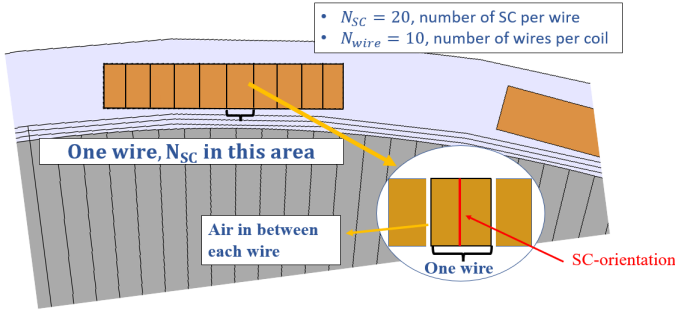
Fig. 11. SC tape orientated radially in the air gap, to potentially minimize AC losses.

E. Materials

"Cobalt Steel Vacoflux 50" was chosen for the stator yoke. BH-curve is illustrated in figure 8. The electric conductivity was set to zero to represent the lamination of the steel in Comsol. Lamination is implemented to remove the high potential eddy current from flowing that might occur in the material. The air gap was set to air, and the magnet BMSG-28 was used.

F. SC implementation

The stator coils contain copper with high electric conductivity. This was done to represent SC implementation simply since a more realistic representation is much more time-consuming. Generally, HA or TA formulation is implemented to obtain a more realistic model. This will be implemented later in the master project.

The SC was placed directly in the air gap. The REBCO SC comes in tapes with a high aspect ratio. They are implemented radially to minimize the effect of the alternating fields in the air gap; see figure 11. With this orientation, most of the magnetic field will interact parallel to the tapes. Hence, the side with the smallest surface area interacts most with the flux density in the air gap. Reducing the threat of potential AC losses in the SC. The tapes are stacked to create wires arranged in multiple turns to complete one coil. The number of SCs per turn and the number of turns were decided to obtain the desired power and current ratings. See table IV.

G. Current phase angle

In FEM simulations of electric motors, it is essential to consider the physical placement and orientation of the rotor and stator to accurately model the electromagnetic forces and torque generated by the motor. The stator currents, which produce the electromagnetic fields that interact with the rotor, should be appropriately aligned with the magnetic flux vector to achieve the maximum possible torque.

To obtain this alignment, the stator currents can be phase shifted to act in phase with the flux vector. This requires a detailed understanding of the machine parameters and the electromagnetic interactions within the motor. A simple FEM simulation can determine the optimal phase shift for the stator currents by examining the torque output as a function of time. By analyzing the torque curve, it is possible to identify the time shift corresponding to the maximum torque point. This information can then be used to adjust the phase of the stator currents to achieve the desired performance.

$$\theta_q = 2\pi \cdot f_e \cdot t_{max} \qquad (21)$$

Where θ_q and t_{max} are the required phase shift angle and the time for maximum torque.

IV. Electromagnetic analysis in COMSOL

An analysis must be conducted to find a design that performs more optimally with the given ratings and machine topology. The machine's performance can be determined by many factors, depending on the purpose and goal of the machine design. As discussed in the introduction, the performance parameters for machines in the aviation industry, that are of greater importance are power density, reliability, and efficiency. Reliability is difficult to analyze in software such as COMSOL, given that there are few parameters to compare reliability performance directly. Discussion and analysis can be made from a study, but direct comparison of results is challenging. Efficiency can be analyzed extensively in FEM software such as COMSOL. A model with accurate loss calculation should be implemented if the efficiency analysis is to be completed. But this focus was dismissed in this project because it is time-consuming and does not fit the objective of the project. As well it will be challenging if a model with TA formulation is also to be implemented. Therefore, power density was sought out to be the main factor for comparing the performance. The plausibility of SC implementation has been discussed and taken into account as well.

A. Winding layout

For the preliminary design, other winding layouts have yet to be compared to the current 12 slots 10 pole layout. To uncover better configurations, a winding layout study is to be conducted. The winding layout can determine the performance of quite a few different parameters. First, it can influence the back EMF(electromotive force) waveform. A good layout can produce a back EMF with less harmonics, yielding better performance. Furthermore, the winding layout determines the distance between the winding pair. This factor can be limiting for superconductors, given that the bending radius of the SC is smaller than for regular Litz wire. The winding layout can also influence torque production, winding losses, and thermal performance. For this analysis, mainly the torque production will be analyzed and discussed.

Designs that use more of the air gap for torque production are to be desired. Therefore four other winding layouts have been tested. For the first one, 30 slots and 10 poles are used with concentrated windings. With more slots in the machine, they will cover more of the air gap, which potentially could mean more torque production. From Emetor, this gave a winding factor of 1. Also, decreasing the number of poles where done to see the effect, generally lower pole count can bring lower weight to the machine. Here two different layouts were tested, 6 poles with both 18 slots and 36 slots. The last one is based on a study done, [7]. Here, 24 slots and 8 poles were used with concentrated windings.

The aim is to obtain the highest power density within the limits of the machine. Therefore, parameters such as a magnet length, number of SC per coil and other geometrical

TABLE V
PRELIMINARY WINDING LAYOUT STUDY

Winding layout	s12p10	s30p10	s24p8	s18p6	s36p6
Steel weight [kg]	52.28	48.95	36.6	66.47	61.28
Magnet weight [kg]	93.3	79.3	61.7	105.43	87.71
Coil weight [kg]	4.6	5.88	2.53	3.9	5.2
Total weight [kg]	150.2	134.1	100.83	175.9	154.2
Power [MW]	2.4	2.48	2.52	2.37	2.62
PTW [kW/kg]	**15.98**	**18.49**	**24.99**	**13.48**	**16.99**
TTW [Nm/kg]	43.33	50.7	67.94	36.95	46.37
Machine length [m]	0.5	0.425	0.275	0.47	0.47
R_{ag} [m]	0.12	0.12	0.12	0.14	0.12

factors have been kept constant for each winding layout. The only adjustments have been made to the stator yoke, air gap radius, and the length of the machine. For the stator yoke, the criteria were set such that the flux density in the cross-section of the stator yoke was under 2 T.

1) 30 slots and 10 poles: For higher slot-number winding layouts, the slots are placed closer together. Making concentrated windings more challenging to implement. Thus a more sensible choice for high slot configuration would be distributed. From Emetor, this winding layout gave a winding factor of 1. The simulation showed that this layout performed better than the original design by reducing the weight from 150 kg to 134 kg, resulting in an active power density of 18.49 kW/kg, see table V. Very little torque ripple was produced as well. However, this design is the one with the most SC used. Due to the cost of SCs, this is a factor which needs to be considered. An important point regarding SC implementation is the bending radius of the material, which could be a problem given the number of slots. But with a distributed layout, this holds well within the limits of the material [35].

2) 18 slots and 6 poles: This configuration produced less power per weight than all the other configurations, table V. High steel and magnet weight resulted in the heaviest design. This design contains the same problem as the original layout, the air gap containing "dead spots" not producing torque. So for this projects machine, a winding layout of 18 slots and 6 poles is not desirable.

3) 36 slots and 6 poles: To use more of the air gap, the number of slots was doubled. Table V shows the performance improved when the slots were doubled, increasing the power density from 13.48 [kW/kg] to 16.99 [kW/kg]. But still lower than the configuration with 30 slots and 10 poles.

Fig. 12. Illustration of 36s6p winding layout. Represented with a third of the full configuration [33].

4) 24 slots and 8 poles: From [7], a 1MW slotless PMSM machine was presented with good results. The machine used a winding layout with 24 slots and 8 poles. In hindsight of these results, this combination also opted to be analyzed. Table V, shows that this combination

has the lowest weight and highest power density by far. Given the distributed configuration, the distance between the winding pairs will not pose a problem for the SC layout. A significant margin to the next one with 24.99 kW/kg, compared to 30 slots and 10 poles with 18.49 kW/kg.

Based on the winding layout study results, the 24 slots and 8 pole configuration showed the best result by far. But this was a preliminary study of the winding layout, meaning each layout could have been optimized better. A few parameter adjustments were implemented to improve the performance, but a thorough analysis was not conducted. This means that some winding layouts could have had the same or better performance. Even though the study that was conducted was just a preliminary study, the 24 slots and 8 pole layout was chosen to be the one used for further investigations.

Fig. 13. Illustration of the winding layout for s30p10, s18p6 and s24p8. The figure represents a fifth of the s30p10 configuration, a third of the s18p6 configuration, and a fourth of the s24p8 configuration [33].

B. Adjusting the R_{ag}

As mentioned in the section "Analytic modeling", the radius of the air gap poses great significance for torque production. Therefore, to find a suitable radius, further analysis must be done in COMSOL. From the analytical approach, a value was found. This value is set as the basis for the simulations. The air gap radius was changed by steps of 0.01 m from $R_{ag} = 0.1$m to $R_{ag} = 0.14$. Also, a greater radius was included to demonstrate the effects when the air gap radius was set to a heightened value. The test was conducted so that the other geometric parameters, the magnet length, coil height, air gap length, and stator yoke, remained the same. A parametric sweep was used to adjust the air gap radius in multiple steps in COMSOL.

Figure 14 demonstrates how the produced mechanical power changes for the different values for the air gap radius. Surprisingly, for higher values than $R_{ag} = 0.14$m, the produced power decreases when the air gap radius increases. This trend contradicts the general machine theory. In equation 14, higher R_{ag} yields higher torque production, increasing the mechanical power as well. For the smallest radius, the torque production is not too far from the lengthier ones. An important factor that equation 14 fails to consider is the working area for torque production. If the coil size is constant and the working area of the torque production is constant, the "dead zones" in the air gap increase. "Dead zones" means areas in the air gap where high torque production does not occur. This element is
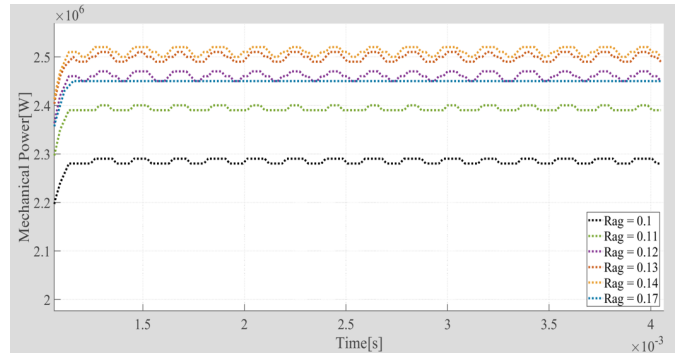

Fig. 14. Mechanical power plotted for the six different scaling values. $R_{ag} = 0.14$m gave the highest value. It can be seen that $R_{ag} = 0.12$ and $R_{ag} = 0.17$ has the same torque production.
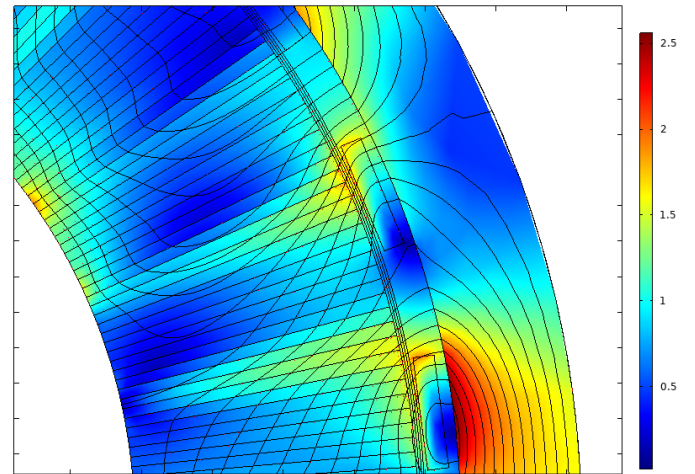

Fig. 15. Flux density plot in COMSOL of the model when the scale factor is set to 1.6. Larger areas in between the coils yields lower torque production.

especially problematic for slotless machines because they do not have teeth. For slotted machines, the teeth distribute the flux from the stator yoke throughout a greater part of the air gap, yielding a smoother distribution compared to slotless. Therefore, without stator teeth, larger areas of low-torque production appear. This phenomenon is illustrated in figure 15.

Table VI shows that the smallest air gap radius, $R_{ag} = 0.10$m, has the best power density. These results occur because the SC coils will cover more of the torque-producing air gap area for a smaller radius. Therefore, more of the magnet

TABLE VI
RESULTS FROM ADJUSTING THE AIR GAP RADIUS

R_{ag}	0.1	0.11	0.12	0.13	0.14	0.17
Steel weight[kg]	27.1	29.46	31.84	34.22	36.61	43.77
Magnet weight[kg]	40.95	46.13	51.32	56.5	62.68	77.24
Mech. Power[MW]	2.28	2.39	2.47	2.5	2.52	2.45
Torque [kNm]	6.23	6.52	6.71	6.8	6.85	6.7
PTW [kW/kg]	32.31	30.59	28.82	26.81	24.75	19.83
TTW [Nm/kg]	88.3	83.46	78.18	73.0	67.27	54.23

11

TABLE VII
RESULTS FROM ADJUSTING THE MAGNET LENGTH

Magnet length	0.025	0.03	0.035	0.04	0.045	0.05
Magnet weight [kg]	27.9	32.5	36.8	40.7	44.4	47.7
Total weight [kg]	57.5	62.1	66.4	70.3	74	77.3
Mech. Power [MW]	1.43	1.77	2.05	2.28	2.45	2.58
PTW [kW/kg]	24.9	28.5	30.9	32.4	33.1	33.37

field from the coils will be taken advantage of. Furthermore, the steel and magnet weight is drastically reduced when the radius is reduced. To keep the high performance of the SC, the bending radius minimum can not be surpassed. But even with the smallest radius, this value is not exceeded [35]. Therefore, given the superior power density of $R_{ag} = 0.10$m this radius is chosen as the one implemented in the design.

C. Magnet adjusting

To search for the optimal design, the best-performing length of the magnets should be found. A value from the analytic approach was found. This value was calculated based on a desired air gap flux density of 0.6 T , equation 17. A standard industry design choice is 0.6 T for the air gap flux density [31]. When the magnet's length increases, the air gap's flux density will increase as well , as demonstrated in equation 17. The increased field will then again increase the generated torque. But longer magnets result in heavier designs. Therefore a parametric sweep was done to find a value that gives the best balance between weight and torque production, resulting in the highest power density. The parametric sweep included steps from $l_m = 0.025$m to $l_m = 0.05$m, with steps of 5 mm.

From table VII it can be seen that for the magnet length of $l_m = 0.05$m, the best power density is produced. Given the small diameter of the machine, long magnets do not seem too realistic. The geometry in COMSOL showed that the magnets were much wider at the top than the bottom for the longest design. This relationship should be avoided since the magnets typically are produced with a more "rectangular" form. But the difference in power density is slight compared to $l_m = 0.045$m and $l_m = 0.04$m. Therefore, magnet length of $l_m = 0.04$m was deemed more reasonable. A potential problem with a greater magnet length producing greater air gap flux density is saturation in the stator yoke. In figure 16, it is demonstrated that for magnet length $l_m = 0.04$m, the flux generated in the stator does not surpass the saturation level in the majority of the stator. The saturation limit is 2.0 T for this material. Hence, the steel losses will not be more significant than for the smaller lengths. In hindsight of these considerations, $l_m = 0.04$m was deemed the optimal magnet length.

D. Adjusting the stator yoke

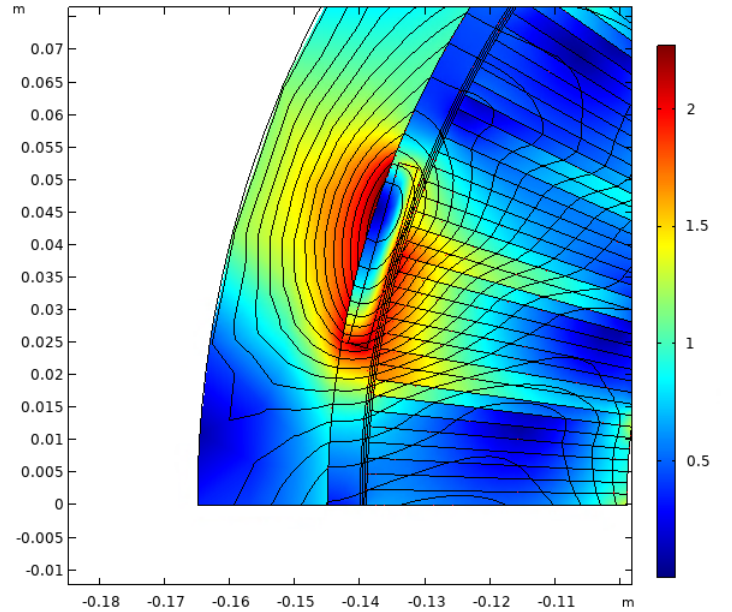Decreasing the stator yoke thickness could be a possible optimization point to increase power density. Thinner yoke

Fig. 16. For magnet length $l_m = 0.04$ m. The flux density in the stator does not seem to surpass the saturation level for the material.
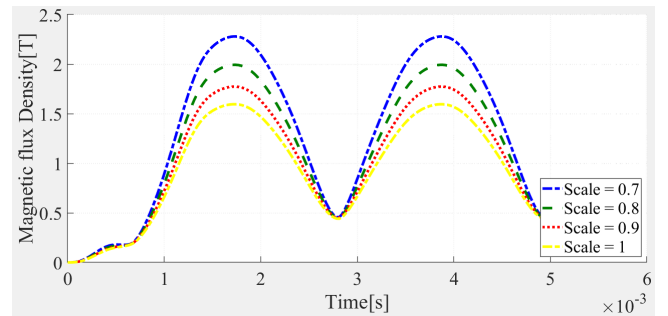

Fig. 17. Cross section of the stator yoke above the C+ coil. Flux density plotted for the four different scale values.
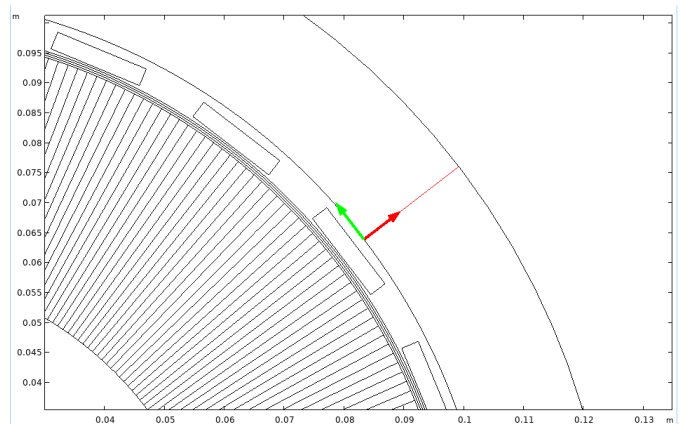

Fig. 18. Cross section where the line average is measured over.

reduces weight, but stator losses should be accounted for as well. If the stator yoke is too thin, saturation will occur in the yoke. For medium-to-high-speed applications such as this one, the losses could be detrimental. Therefore it should be tested to determine how thin the yoke can be without adding losses to the design. As mentioned before, the steel used for this model saturates around 2 T.

The tuning of the stator yoke has been done accordingly. The criteria for an acceptable yoke thickness are determined by the yoke cross-section average flux density not exceeding 2T. Over the coils, the most significant flux density occurred, see figure 18. Therefore the cross-section above the coils where measured. Figure 17 demonstrates how the flux density in the cross-section changes for different yoke thicknesses. When the yoke thickness is lowest, the flux density field exceeds the limit. For the scaling value of 0.8, the flux density slightly exceeds the limit, and for 0.9, the field has a good margin to the limit. Therefore, a value of 0.85 was considered the best scaling value. This resulted in a yoke thickness of 17 mm.

V. TA-FORMULATION IMPLEMENTED IN COMSOL

When a more optimal design for the machine has been found, more elements must be analyzed to see if the design would be realistic in practice. Accessing a more realistic model of the machine makes it so that it is possible to determine the behavior of the machine at different operating temperatures. Detrimental for the design of an SC machine is the AC losses in the SC material. Given the cryogenic temperatures the material operates in, the penalty of cooling for the losses is far greater than for ambient temperatures. In order to access the AC losses of the superconducting material, TA formulation is implemented in the COMSOL model, this formulation is able to handle the high aspect ratio of the SC strips. HA formulation is a common alternative to formulating the AC losses, but due to the high computational power needed in order to solve the equations [36] , TA formulation is a more attractive option for this model. Its fast computing time is mostly due to the assumptions added to the calculation, as mentioned in the "Theory" section.

The TA formulation consists of two different physics in the COMSOL working together. The A-formulation is implemented through the *Magnetic fields(mf)* physics. Also, the *rotating machinery physics(rmm)* can be used. But due to difficulties for the model to converge and the computational time due to the rotating mesh, the *Magnetic fields* physics is preferred. The ability of the segmented rotor implemented to emulate the rotating magnetic field of *rmm*, makes the *Magnetic Fields* able to simulate the same scenarios as the *rmm* but with lower computational time.

The T formulation is implemented through the *general form PDE* physics, with the use of equation 5.The following assumptions have been made in the formulation:

- Formulated as an infinitely thin strip
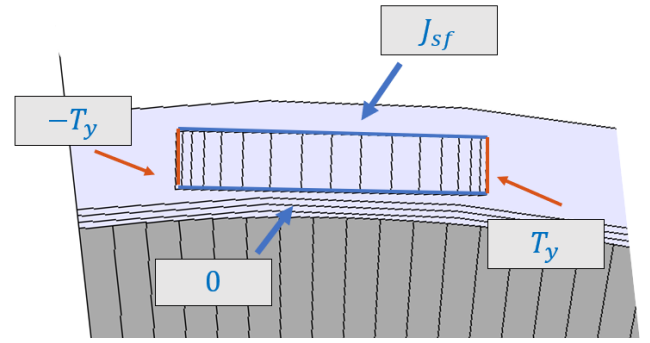- Infinetly long in the z direction

Fig. 19. The boundary condition implementation of the T formulation in COMSOL.

- Current only flows in the z direction

In order to reduce computing time even further, the SC coil where represented in a more simple manner. A homogenized approach is used, and it uses a bulk instead of each individual tape. Inside the bulk, some of the tapes are calculated and furthermore interpolated in between them. The implementation is based of the approach presented in [26].

The current in the T-formulation is set up by a surface current density applied to the boundaries on the side of the TA coil. The outward facing side is set as J_{sf}, see equation 8, and the inward facing side is set as zero. For the boundaries on top and bottom of the coil, Neumanns boundary condition have been used, equation 11. T_y is applied to the top will $-T_y$ is applied to the bottom, see figure 19.

A. Segmenting the rotor

Due to the extreme demand for computing power in TA formulation, the rotor was segmented to save computing time and improve convergence. The Halbach array was replaced with smaller non-rotational segments, which rotate the magnetization and not the mesh. See figure 20. This method is based on the work in [37]. Both accuracy and computational speed are to be desired. If the accuracy goes below an acceptable level, the increased computational rate will not matter. In the original work, the model can achieve accuracy above 99% compared to the rotating model. Each fine segment is magnetized from a function dependent on time and segment number; implemented through equation 22. The magnet field generated from the Halbach is sinusoidal with higher harmonics. Therefore, to assemble the real model, this also has to be accounted for, eq. 23. From the original method [37], it was discovered that the 1st, 9th, and 11th harmonics were the dominating ones in the air gap flux density. The coefficients used were found through Fourier analysis of the air gap flux density. The values used can be seen in table VIII.
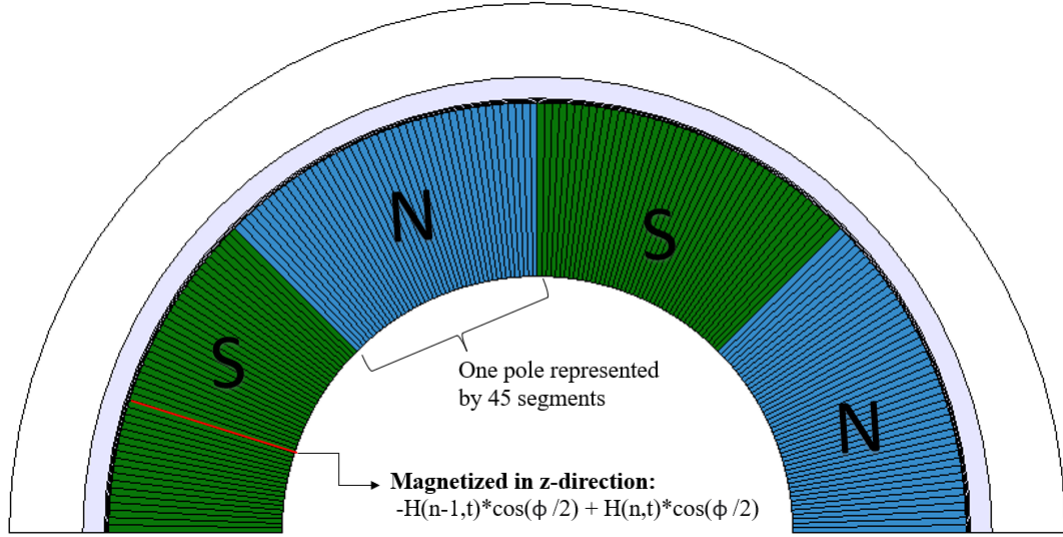
13

Fig. 20. Visual representation of the segmenting of the rotor.

TABLE VIII
CONSTANTS USED FOR SEGMENTING

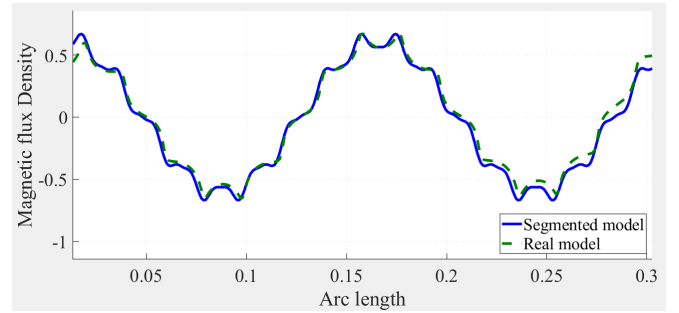| Description	Symbol	Value	Unit
Angular freq. of magnets	ω	1832.6	rad/s
Angle per segment	θ_{PM}	0.087	rad
Surface H-field	H_k	1.09E6	A/m
Harmonic number 1	n_1	1	–
Harmonic number 2	n_2	9	–
Harmonic number 3	n_3	11	–
1st harmonic coefficient	a_1	1.298	–
9th harmonic coefficient	a_2	-0.238	–
11th harmonic coefficient	a_3	0.126	–

Fig. 21. Air gap flux density plotted over the arc length for both the real model and the segmented model.

$$H(a_i, n_i, n) = a_i \cdot sin(n_i\omega t + n_i n(\theta_s + 0.5) + n_i\theta_{PM}) \quad (22)$$

$$H_s = H_k(H(a_1, n_1, n) + H(a_2, n_2, n) + H(a_3, n_3, n)) \quad (23)$$

Here a_i, n_i, ωt and θ_{PM} are the ith harmonic coefficient, harmonic number, rotor frequency and angle per segment.

Given that in electrical machines, the tangential part of the air gap flux density contributes to torque production. Therefore, the rotor's segmented representation should only resemble the air gap flux density in the tangential direction. Hence these functions are magnetizing so that the tangential air gap flux density is as similar as possible to the original rotor. As shown in figure 21, when the coils are neglected, the tangential component of the air gap flux density is similar to the segmented model. The magnet losses will not be calculated and analyzed. That is due to incorrect magnetic fields inside the magnets. Due to the segmenting, only the field produced in the tangential direction is replicated from the real field. Yielding in an incorrect field inside the magnets. Given this, the magnet losses are not to be considered.

To calculate the AC losses in the SC material the general equation for volumetric loss density is used:

$$Q = J \cdot E \quad (24)$$

In COMSOL this equation is integrated over the surface area of the TA implemented coil.

B. Simulation results

After implementing the TA formulation successfully, the coil current for the TA coil had an equal phase and amplitude as the non-TA coils and the torque produced was similar to the Non-TA model. The geometry and power ratings are the same for these simulations as for the Non-TA model. From figure 23, the AC losses for the TA coil are plotted. It can be seen that the losses follow the coil current and have their peak around $t = 0.033s$ with $250W$. The plotted AC losses are only from one coil. Adding the AC
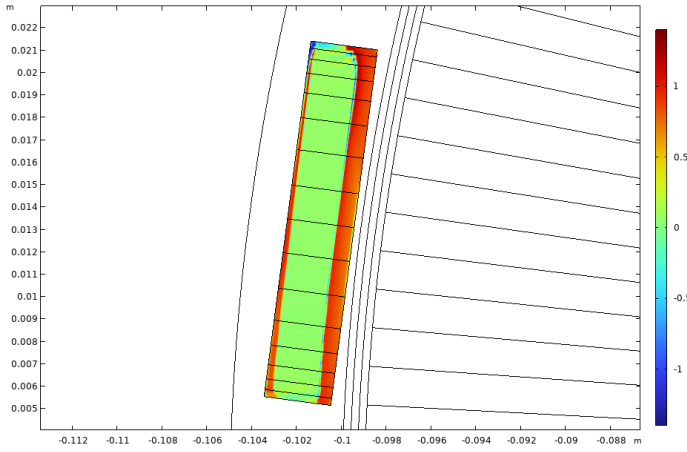
Fig. 22. Surface plot for the current density in the z-direction relative to the critical current density at t=0.3482s, the time for peak phase A current. The current density at the sides is 20-30 times greater than the density in the middle area.
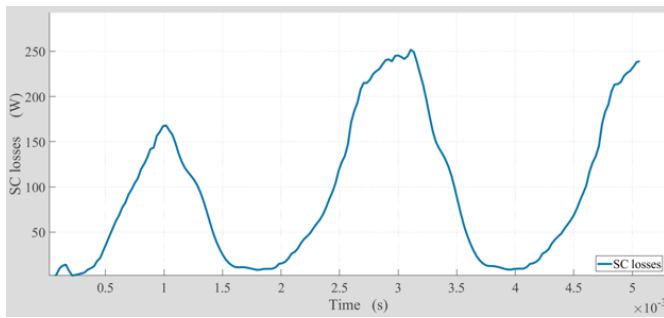

Fig. 23. The AC losses for the TA coil plotted over the simulation period with 30% current loading.

losses from the remaining 23 coils, total AC losses are in the kW range. For a machine with mechanical power production of 2.5 MW, these losses are relatively small. But as mentioned in the theory section, these are cold losses, meaning the penalty is quite high for removing them at low temperatures.

Figure 22 shows the current density distribution. The results are as expected for an HTS tape, in [38] similar results are showed. The current flows in the same direction on both sides, which is essential to note. If the current had been in opposite direction in extensive areas of the coil, circulating currents that do not contribute to power would weaken the performance. The current density exceeds the critical current density calculated by a Kim-like model on the sides of the tape by a factor of up to 1.1. High relative current densities can be a significant contribution to AC losses. Decreasing the current loading could reduce the current density below the critical one for a greater part of the coil.

The layer with increased current density is more prominent on the side of the tape closest to the magnets. This is because the side contains a more prominent applied
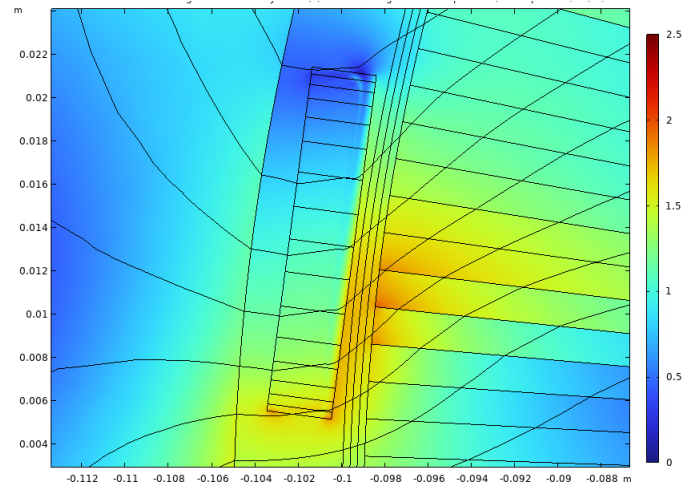

Fig. 24. Surface plot of the magnetic flux density at t=0.005. The field lines pass over the tape with an angle, meaning the applied magnetic field hits the tape with an angle. Potential increasing the AC losses.
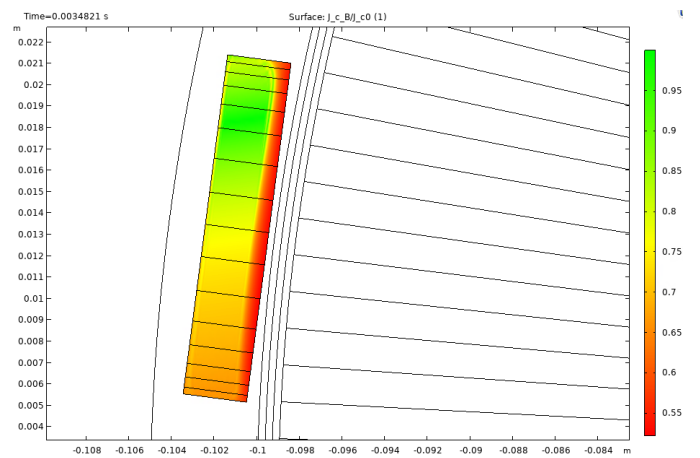

Fig. 25. Surface plot showing the relationship between the constant critical current density and the one calculated by the Kim-like model , t=0.03482s. The area closest to the magnet are a lot more affect than the rest of the coil.

field due to the magnetic field from the magnets interacting more on the inward-facing side than the opposite side. Figure 25 shows the effect of the applied magnetic field on the critical current density. The side facing the magnets has a decreased critical current density, down to a factor of 0.5. The lower critical current density significantly weakens the performance of the SC in that region. This phenomenon is mainly due to two factors contributing to low critical current densities on the side of the tape. Firstly, as shown in figure 24, the field hits the tape side with an angle and not parallel to the tapes. When the applied field hits the tape with an angle it interacts with a greater surface area on the tape, yielding greater impact. Secondly, the SC in the slotless design is more exposed to external fields than in the slotted topology, and this is mainly due to no shielding of external fields in a slotless machine. These two factors, combined, result in lower critical current density in the affected areas, yielding more significant losses.
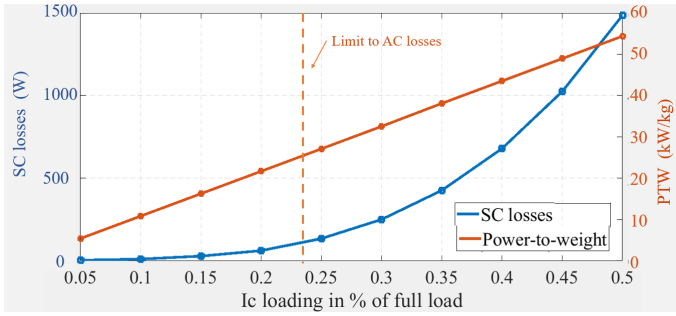
15

Fig. 26. SC losses and PTW plotted for each current loading. For the losses, the peak instantaneous loss was used, and not the average, to compare for each loading. The dotted line presents the cut off point for the losses around 100W. These simulations were performed at 60K.

The phenomenons showed in figures 22 and 25 illustrates the most detrimental problems with the implementation of SC in a slotless machine. With them occurring in the same regions as well, makes it so that in order to design a feasible motor these effects have to be minimized.

1) Changing the current loading: A parameter study was done in COMSOl, where the current loading of SC was changed. Figure 26 demonstrates how the current loading influences both the SC losses and PTW. For higher current loadings the losses increases exponentially, while the torque production only increases linearly. The average losses over the electrical period could also have been used for the plot, but given that the all the instantaneous losses had the same graph form, the peak was used in order to highlight the worst operating condition of the machine. The current loading is defined by the following equation:

$$I_{load,\%} = \frac{I_{peak}}{I_c} \qquad (25)$$

Here I_{peak} is the amplitude of the sinusoidal current in one SC, while I_c is the peak critical current in one SC given by the manufacture [39].
In [40], expected losses for SC in mega-watt scale motors are presented. It is in the range of 50W to 200W. Since in this analysis, only the AC losses in the SC layer are taken into account, the losses plotted are desired to be under 100W.

The results shows that a low current loading is needed in order to minimize the losses. The original current loading was set to 30%, as plotted in figure 23 this current loading yielded high instantaneous losses in the TA coil. For 20% current loading, the losses decreased by 25% while still having PTW over $20 \frac{kW}{kg}$. Reducing the current loading to 20% shows better potential for dealing with the negative consequences of SC implementation.

2) Temperature dependency: As discussed in the theory section, the performance of SC is dependant on the temperature of the material. From the figures 2 and 3 it is visualized
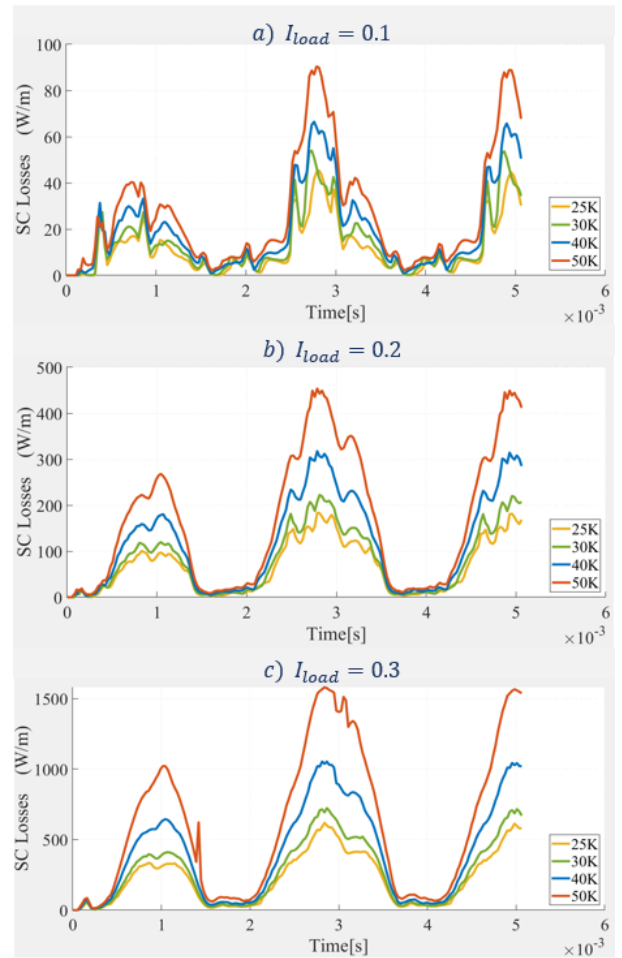

Fig. 27. Instantaneous losses per length of the machine for the material with four different temperatures, ranging from 25K to 50K. Three different plots were the current loading was adjusted. Values used were $I_{load} = 10\%$, $I_{load} = 20\%$ and $I_{load} = 30\%$.

that for higher temperatures the critical values for current density and applied magnetic fields decreases. So far the model have assumed operating temperature of 60 kelvin. This temperature is in the higher region for operating temperature for HTS, where the limit is 77 kelvin. LH2 is a potential coolant for the machine, reaching temperatures in the range of the 20 to 30 kelvin. In hindsight of this discussion, a parameter study were conducted to analyze the influence of temperature to performance of the machine. So far the temperature have been implemented in COMSOL through Kims model, which calculates the critical temperature of the material. The constants for the model is temperature dependant. Therefore, 4 different simulation have been conducted where the constants was changed. The constants have been handed out from my supervisor, see table IX for the constants. Current loading was set to 20%

Figure 27 visualizes the instantaneous losses for four temperatures at three current loadings. Major differences can be seen between the different temperatures, especially for the

16

TABLE IX
KIM-LIKE MODEL CONSTANTS FOR DIFFERENT TEMPERATURES

Temperature	25K	30K	40K	50K	60K
γ	18.051	13.996	11.39	12.092	4.3985
B_0	0.5	0.305	0.75	0.1	0.1
α	1	0.667	0.334	0.2012	0.2307
$J_c\ [A/m^2]$	3.72e11	3.268e11	2.54e11	1.97e11	1.474e11

highest current loading. SC's performance is generally very dependent on the temperature because the critical current density decreases rapidly when the temperature increases; see table IX.

A trend can be seen from the plots when the current loading decreases. For the lower current loading, the difference between the temperatures decreases. The demand on the SC with this current loading is low; therefore, decreasing the temperature will not reduce the losses substantially. When the temperature rises, the critical current density in the material decreases; see figure 3. But if the current density does not exceed this limit more for the higher temperature, the losses will not increase substantially. For the operation of the machine, these considerations are of great importance. For higher current loading, the temperature is more detrimental to the performance of the SC tapes.

In [40], table 2, the effect of temperature on heat removal is listed. A notable difference between the temperatures can be seen. So, even though the lower temperatures yield lower losses, these losses give a higher penalty. Therefore, the difference between the temperatures is, in reality, lower than the loss plots demonstrate, given the higher penalty for the losses. The loss removal cost will most likely be higher for higher temperatures, but this is a factor that needs to be considered when deciding the operating conditions for the machine.

VI. FINISHED MODEL

After the analysis of the geometrical parameters and the TA formulation analysis, a optimized design was found. The first analysis determined the winding layout, air gap radius, magnet height and stator yoke thickness was determined, see table XI. From the TA formulation analysis, the current loading was set 20%. This combined resulted in a design that can be seen in figure 29. Performance parameters are demonstrated in table X. The design yielded mechanical power of $1.52MW$ and a power density of 24.7 kg/kW. From figure 30 the torque production is demonstrated over the simulation period. Small torque ripple, 0.3%, can been seen, this is to be expected given the slotless topology. The magnetic flux distribution can be seen in figure 31.
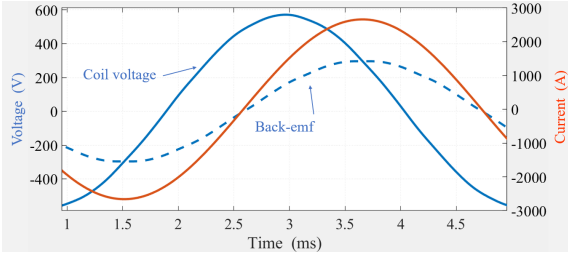

Fig. 28. Injected sinusoidal current phase current compared to coil voltage at rated condition and back-emf produced in the coils.
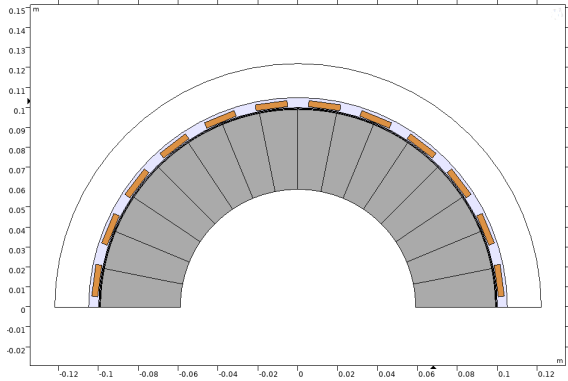

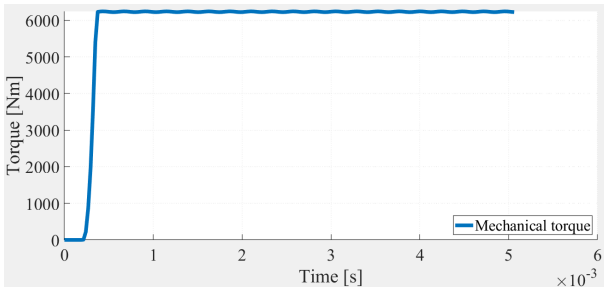Fig. 29. Finished design in COMSOL, see table for exact measurements.

Fig. 30. Mechanical torque from the finished model.

TABLE X
PERFORMANCE PARAMETER

Description	Symbol	Value	Unit
Average mechanical power	P_m	1.53	MW
Speed	n_{rpm}	3500	rpm
Electrical frequency	f_{el}	233	Hz
AC losses [1]	P_{SC}	78,5	W
Magnet weight	m_{PM}	40.95	kg
Steel weight	m_{fe}	18.43	kg
SC weight	m_{SC}	2.53	kg
Active total weight	m_{tot}	61.91	kg
Average torque	T_{mec}	4350	Nm
Torque ripple	ΔT_m	0.3	%
Active power-to-weight	PTW_{act}	24.7	kW/kg
Active torque-to-weight	TTW_{act}	70.26	Nm/kg
RMS phase current	I_{rms}	1254	A
RMS phase voltage	U_{ph}	265	V

[1] AC losses is at 60K and for 20% current loading in one coil.

TABLE XI
FINAL GEOMETRICAL PARAMETERS

| Description	Symbol	Value	Unit
Air gap radius	R_{ag}	0.1	m
Inner machine radius	R_i	0.0595	m
Outer machine radius	R_o	0.122	m
Machine length	L	0.275	m
Air gap length w/ coil	l_{ag}	0.01	m
Air gap length w/o coil	$l_{ag,1}$	1	mm
Stator yoke height	h_{ys}	0.012	m
Number of slots	N_s	24	—
Poles	p	8	—
Magnet length	l_m	0.04	m
SC in a wire	N_{SC}	20	—
Wires per coil	N_w	10	—
Number of SC	N	200	—
Area of coil	A_{coil}	4.8E-5	m^2
Height of coil	h_{coil}	0.016	m
Width of coil	w_{coil}	3	mm
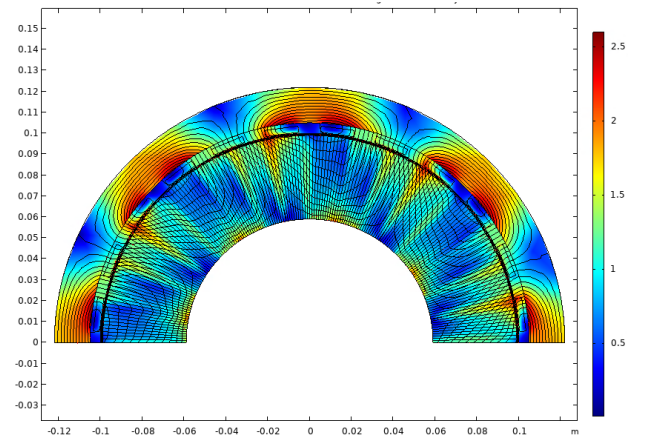
Fig. 31. Surface plot of the flux density of the finished design at t=0.025.Even flux distribution in the stator yoke.

VII. CONCLUSION

The study has presented a finalized design of a megawatt scaled superconducting slotless PMSM for aviation applications. Electromagnetic analysis in COMSOL achieved the deduction of optimal geometrical parameters. In slotless machines, the size and distance between each coil hold significant importance for the power density parameter, as their reach along a substantial part of the circumference ensures efficient utilization of the induced current. Notably, when scaling the air gap radius, it was observed that the highest values led to decreased torque production, contradicting theoretical expectations. Meaning the lower air gap radius demonstrated excellent power density. This observation was further reinforced in the investigation of winding layouts, wherein configurations with higher slot numbers generally outperformed those with fewer slots. With the implementation of a Halbach array, weight reduction was achieved, given the lack of a rotor yoke.

Introducing the TA formulation enabled access to the AC losses in the superconductors. The performance of SCs was found to be heavily influenced by the flux density field within the air gap. The region in the SCs closest to the magnets showed lower critical current density, resulting in increased losses in these areas. The highest current densities were found on the sides of the SC tapes. These two effects combined resulted in most of the SC losses. Furthermore, the operating temperature and current loading influenced loss generation. Therefore, careful selection of these values is crucial. By setting the current loading to 20% and operating temperature to 60 K, the losses were maintained within an acceptable range of 78W per coil.

Finally, the designed motor achieved a power density of 24.7 kW/kg, surpassing the industry's 20 kW/kg goal. These results exhibit great promise for integrating superconductors in aviation applications, but further analysis needs to be conducted, given the number of factors neglected in this study.

VIII. FURTHER WORK

The following list mentions the potential further work based of the results of this report:

- Implement steel losses into the model to demonstrate the total losses and efficiency of the machine.
- Add magnet losses and research potential risk of demagnetization due to the high magnetic fields from the SC coils.
- Improve the placement of SC coils and investigate possible solutions to protect the SC from the high air gap fields.
- Investigate potential coolants and how cooling would be implemented in practice.
- Further analysis of different winding layouts, where each layout is optimized.
- Research in how this machine would interact with the rest of the system, inverter, battery, motor control etc.

REFERENCES

[1] C. Gerada, M. Galea, and A. Kladas, "Electrical machines for aerospace applications," in *2015 IEEE Workshop on Electrical Machines Design, Control and Diagnosis (WEMDCD)*, Mar. 2015, pp. 79–84.

[2] B. A. Adu-Gyamfi and C. Good, "Electric aviation: A review of concepts and enabling technologies," *Transportation Engineering*, vol. 9, p. 100134, Sep. 2022. [Online]. Available: https://www.sciencedirect.com/science/article/pii/S2666691X2200032X

[3] D. Talebi, M. Gardner, S. V. Sankarraman, A. Daniar, and H. Toliyat, "Electromagnetic Design Characterization of a Dual Rotor Axial Flux Motor for Electric Aircraft," May 2021, pp. 1–8.

[4] R. Mellerud, J. Nøland, and C. Hartmann, "Preliminary Design of a 2.5-MW Superconducting Propulsion Motor for Hydrogen-Powered Aviation," in *2022 International Conference on Electrical Machines (ICEM)*, Sep. 2022, pp. 1404–1410, iSSN: 2381-4802.

[5] V. Madonna, P. Giangrande, C. Gerada, and M. Galea, "Thermal analysis of fault-tolerant electrical machines for aerospace actuators," *IET Electric Power Applications*, vol. 13, Jul. 2019.

[6] "Mission and Values | Clean Aviation." [Online]. Available: https://www.clean-aviation.eu/mission-and-values

[7] F. Grilli, T. Benkel, J. Hänisch, M. Lao, T. Reis, E. Berberich, S. Wolfstädter, C. Schneider, P. Miller, C. Palmer, B. Glowacki, V. Climente-Alarcon, A. Smara, L. Tomkow, J. Teigelkötter, A. Stock, J. Büdel, L. Jeunesse, M. Staempflin, G. Delautre, B. Zimmermann, R. v. d. Woude, A. Perez, S. Samoilenkov, A. Molodyk, E. Pardo, M. Kapolka, S. Li, and A. Dadhich, "Superconducting motors for aircraft propulsion: the Advanced Superconducting Motor Experimental Demonstrator project," *Journal of Physics: Conference Series*, vol. 1590, no. 1, p. 012051, Jul. 2020, publisher: IOP Publishing. [Online]. Available: https://iopscience.iop.org/article/10.1088/1742-6596/1590/1/012051/meta

[8] C. Oberly, "Lightweight superconducting generators for mobile military platforms," in *2006 IEEE Power Engineering Society General Meeting*, Jun. 2006, pp. 8 pp.–, iSSN: 1932-5517.

[9] "HTS machines as enabling technology for all-electric airborne vehicles - IOPscience." [Online]. Available: https://iopscience.iop.org/article/10.1088/0953-2048/20/8/005

[10] K. S. Haran, S. Kalsi, T. Arndt, H. Karmaker, R. Badcock, B. Buckley, T. Haugan, M. Izumi, D. Loder, J. W. Bray, P. Masson, and E. W. Stautner, "High power density superconducting rotating machines—development status and technology roadmap," *Superconductor Science and Technology*, vol. 30, no. 12, p. 123002, Dec. 2017. [Online]. Available: https://iopscience.iop.org/article/10.1088/1361-6668/aa833e

[11] P. Masson, D. Soban, E. Upton, J. Pienkos, and C. Luongo, "HTS motors in aircraft propulsion: design considerations," *IEEE Transactions on Applied Superconductivity*, vol. 15, no. 2, pp. 2218–2221, Jun. 2005, conference Name: IEEE Transactions on Applied Superconductivity.

[12] P. Masson and C. Luongo, "High power density superconducting motor for all-electric aircraft propulsion," *IEEE Transactions on Applied Superconductivity*, vol. 15, no. 2, pp. 2226–2229, Jun. 2005, conference Name: IEEE Transactions on Applied Superconductivity.

[13] H. W. Cho, M. Feddersen, and K. S. Haran, "Design and analysis of air-core superconducting generator for wind power applications," *Journal of Physics: Conference Series*, vol. 1054, no. 1, p. 012083, Jul. 2018, publisher: IOP Publishing. [Online]. Available: https://dx.doi.org/10.1088/1742-6596/1054/1/012083

[14] "FUNDAMENTALS OF SUPERCONDUCTORS." [Online]. Available: https://technicalreports.ornl.gov/m/ornlm3063r1/pt3.html

[15] "p2000d267g24001.jpg (455×491)." [Online]. Available: https://nap.nationalacademies.org/openbook/0309095824/xhtml/images/p2000d267g24001.jpg

[16] M. Zaid, *High temperature superconductors [HTS] for energy applications*, 2012.

[17] Z. Melhem, *High Temperature Superconductors (HTS) for Energy Applications*. Elsevier, Dec. 2011, google-Books-ID: DJVwAgAAQBAJ.

[18] M. Ainslie, "Transport AC loss in high temperature superconducting coils," Ph.D. dissertation, May 2012.

[19] "Next Generation More-Electric Aircraft: A Potential Application for HTS Superconductors | IEEE Journals & Magazine | IEEE Xplore." [Online]. Available: https://ieeexplore.ieee.org/document/5153109

[20] M. Yazdani-Asrami, A. Sadeghi, and M. D. Atrey, "Selecting a cryogenic cooling system for superconducting machines: General considerations for electric machine designers and engineers," *International Journal of Refrigeration*, vol. 140, pp. 70–81, Aug. 2022. [Online]. Available: https://www.sciencedirect.com/science/article/pii/S0140700722001554

[21] J. K. Nøland, R. Mellerud, and C. Hartmann, "Next-Generation Cryo-Electric Hydrogen-Powered Aviation: A Disruptive Superconducting Propulsion System Cooled by Onboard Cryogenic Fuels," *IEEE Industrial Electronics Magazine*, vol. 16, no. 4, pp. 6–15, Dec. 2022, conference Name: IEEE Industrial Electronics Magazine.

[22] J. Gieras, "Superconducting Electrical Machines State of the Art," *Przeglad Elektrotechniczny*, vol. 85, pp. 1–19, Dec. 2009.

[23] M. Komiya, T. Aikawa, H. Sasa, S. Miura, M. Iwakuma, T. Yoshida, T. Sasayama, A. Tomioka, M. Konno, and T. Izumi, "Design Study of 10 MW REBCO Fully Superconducting Synchronous Generator for Electric Aircraft," *IEEE Transactions on Applied Superconductivity*, vol. 29, no. 5, pp. 1–6, Aug. 2019, conference Name: IEEE Transactions on Applied Superconductivity.

[24] H. Sasa, M. Iwakuma, K. Yoshida, S. Sato, T. Sasayama, T. Yoshida, K. Yamamoto, S. Miura, A. Kawagoe, T. Izumi, A. Tomioka, M. Konno, Y. Sasamori, H. Honda, Y. Hase, M. Syutoh, S. Lee, S. Hasuo, M. Nakamura, T. Hasegawa, Y. Aoki, and T. Umeno, "Experimental Evaluation of 1 kW-class Prototype REBCO Fully Superconducting Synchronous Motor Cooled by Subcooled Liquid Nitrogen for E-Aircraft," *IEEE Transactions on Applied Superconductivity*, vol. 31, no. 5, pp. 1–6, Aug. 2021, conference Name: IEEE Transactions on Applied Superconductivity.

[25] H. Zhang, Z. Wen, F. Grilli, K. Gyftakis, and M. Mueller, "Alternating Current Loss of Superconductors Applied to Superconducting Electrical Machines," *Energies*, vol. 14, no. 8, p. 2234, Jan. 2021, number: 8 Publisher: Multidisciplinary Digital Publishing Institute. [Online]. Available: https://www.mdpi.com/1996-1073/14/8/2234

[26] F. Huber, W. Song, M. Zhang, and F. Grilli, "The T-A formulation: an efficient approach to model the macroscopic electromagnetic behaviour of HTS coated conductor applications," *Superconductor Science and Technology*, vol. 35, no. 4, p. 043003, Apr. 2022. [Online]. Available: https://iopscience.iop.org/article/10.1088/1361-6668/ac5163

[27] F. Grilli, E. Pardo, A. Stenvall, D. N. Nguyen, W. Yuan, and F. Gömöry, "Computation of Losses in HTS Under the Action of Varying Magnetic Fields and Currents," *IEEE Transactions on Applied Superconductivity*, vol. 24, no. 1, pp. 78–110, Feb. 2014, conference Name: IEEE Transactions on Applied Superconductivity.

[28] R. P. Praveen, M. H. Ravichandran, V. T. Sadasivan Achari, V. P. Jagathy Raj, G. Madhu, and G. R. Bindu, "A Novel Slotless Halbach-Array Permanent-Magnet Brushless DC Motor for Spacecraft Applications," *IEEE Transactions on Industrial Electronics*, vol. 59, no. 9, pp. 3553–3560, Sep. 2012, conference Name: IEEE Transactions on Industrial Electronics.

[29] A. Yoon, X. Yi, J. Martin, Y. Chen, and K. Haran, "A high-speed, high-frequency, air-core PM machine for aircraft application," in *2016 IEEE Power and Energy Conference at Illinois (PECI)*, Feb. 2016, pp. 1–4.

[30] R. Ilka, Y. Alinejad-Beromi, H. Yaghobi, and H. Asgharpour-Alamdari,

[31] "Design of Slotless BLDC Motor for Eliminating Cogging Torque," 2014.

[31] J. Pyrhonen, T. Jokinen, and V. Hrabovcova, "Design of Rotating Electrical Machines."

[32] D. Lee, T. Balachandran, N. Salk, J. Schuh, A. Yoon, P. Xiao, Y. Yu, S. Lin, P. Powell, and K. K. Haran, "Design and Prototype of a High Power Density Slotless PMSM for Direct Drive Aircraft Propulsion," in *2021 IEEE Power and Energy Conference at Illinois (PECI)*, Apr. 2021, pp. 1–6.

[33] "Emetor - Electric motor winding calculator." [Online]. Available: https://www.emetor.com/windings/

[34] R. Mellerud, "Report from Runar- preliminary."

[35] "2G HTS Wire Specification | SuperPower." [Online]. Available: https://www.superpower-inc.com/specification.aspx

[36] T. Benkel, M. Lao, Y. Liu, E. Pardo, S. Wolfstadter, T. Reis, and F. Grilli, "*T–A* -Formulation to Model Electrical Machines With HTS Coated Conductor Coils," *IEEE Transactions on Applied Superconductivity*, vol. 30, no. 6, pp. 1–7, Sep. 2020. [Online]. Available: https://ieeexplore.ieee.org/document/8967126/

[37] C. Hartmann, R. Mellerud, J. K. Nøland, and R. Nilssen, "A Static FEA Framework for Fast Analysis of HTS Armature Windings in AC Superconducting SMPM Machines," *IEEE Transactions on Energy Conversion*, pp. 1–11, 2023, conference Name: IEEE Transactions on Energy Conversion.

[38] T. Yazawa, J. Rabbers, O. Shevchenko, B. Ten Haken, H. Ten Kate, and H. Maeda, "Modeling the current distribution in HTS tapes with transport current and applied magnetic field," *IEEE Transactions on Appiled Superconductivity*, vol. 9, no. 2, pp. 797–800, Jun. 1999. [Online]. Available: http://ieeexplore.ieee.org/document/783417/

[39] "Fujikura Ltd." [Online]. Available: https://www.fujikura.co.jp/

[40] M. Gouge, J. Demko, B. Mcconnell, and J. Pfotenhauer, "Cryogenics Assessment Report," Jan. 2002.

[41] Z. Zhang, W. Geng, Y. Liu, and C. Wang, "Feasibility of a new ironless-stator axial flux permanent magnet machine for aircraft electric propulsion application," *CES Transactions on Electrical Machines and Systems*, vol. 3, no. 1, pp. 30–38, Mar. 2019, conference Name: CES Transactions on Electrical Machines and Systems.

[42] P. Masson, M. Breschi, P. Tixador, and C. Luongo, "Design of HTS Axial Flux Motor for Aircraft Propulsion," *Applied Superconductivity, IEEE Transactions on*, vol. 17, pp. 1533–1536, Jul. 2007.

[43] A. Colle, T. Lubin, S. Ayat, O. Gosselin, and J. Leveque, "Test of a Flux Modulation Superconducting Machine for Aircraft," *Journal of Physics: Conference Series*, vol. 1590, no. 1, p. 012052, Jul. 2020. [Online]. Available: https://iopscience.iop.org/article/10.1088/1742-6596/1590/1/012052

[44] M. Filipenko, L. Kühn, T. Gleixner, M. Thummet, M. Lessmann, D. Möller, M. Böhm, A. Schröter, K. Häse, J. Grundmann, M. Wilke, M. Frank, P. v. Hasselt, J. Richter, M. Herranz-Garcia, C. Weidermann, A. Spangolo, M. Klöpzig, P. Gröppel, and S. Moldenhauer, "Concept design of a high power superconducting generator for future hybrid-electric aircraft," *Superconductor Science and Technology*, vol. 33, no. 5, p. 054002, Mar. 2020, publisher: IOP Publishing. [Online]. Available: https://dx.doi.org/10.1088/1361-6668/ab695a

[45] K. Sivasubramaniam, T. Zhang, M. Lokhandwalla, E. Laskaris, J. Bray, B. Gerstler, M. Shah, and J. Alexander, "Development of a High Speed HTS Generator for Airborne Applications," *Applied Superconductivity, IEEE Transactions on*, vol. 19, pp. 1656–1661, Jul. 2009.

[46] K. S. Haran, D. Loder, T. O. Deppen, and L. Zheng, "Actively Shielded High-Field Air-Core Superconducting Machines," *IEEE Transactions on Applied Superconductivity*, vol. 26, no. 2, pp. 98–105, Mar. 2016, conference Name: IEEE Transactions on Applied Superconductivity.

[47] R. H. Jansen, P. Kascak, R. Dyson, A. Woodworth, J. Scheidler, A. D. Smith, E. Stalcup, T. Tallerico, Y. de Jesus-Arce, D. Avanesian, K. Duffy, P. Passe, and G. Szpak, "High Efficiency Megawatt Motor Preliminary Design," in *2019 AIAA/IEEE Electric Aircraft Technologies Symposium (EATS)*, Aug. 2019, pp. 1–13.

[48] H.-W. Cho, T.-K. Bang, J.-I. Lee, K.-H. Shin, H.-S. Lee, J.-S. Hur, and K. S. Haran, "Design and Preliminary Experiments of a Rotating Armature Partial Superconducting Air-Core Generator," *IEEE Transactions on Applied Superconductivity*, vol. 32, no. 6, pp. 1–5, Sep. 2022, conference Name: IEEE Transactions on Applied Superconductivity.

A. Tables from COMSOL

In the following section the most important parameters and functions are presented as screenshots from the COMSOL model. Figures 32-38.

Name	Expression	Value	Description
R_ag	0.10[m]	0.1 m	Air gap radius
R_ro	R_ag-g/2-l_m	0.0595 m	Rotor outer radius
R_si	R_ag+0.0015 +w_coil	0.1045 m	Stator inner radius
R_ri	R_ro-(w_bi*1.5-l_m)	0.0815 m	Rotor inner radius (Not in use)
R_so	R_si+w_bi	0.1165 m	Stator outer radius
alpha_m	1/36	0.027778	Magnet width as percentage of pole pitch
g	1 [mm]	0.001 m	Air gap length
L	0.25[m]*1.1	0.275 m	Machine length
l_m	0.04 [m]	0.04 m	Magnet length
N_ph	3	3	#phases
N_s	12	12	#slots
theta_p	360[deg]/p	0.7854 rad	Angular pole pitch
theta_s	360[deg]/N_s	0.5236 rad	Angular slot pitch
w_bi	0.012[m]	0.012 m	Back iron width
N_sectors	2	2	#Sectors
p	8	8	number of poles
k	0.01[m]	0.01 m	spacing for slots
scale	0.7	0.7	scaling for the geometry

Fig. 32. Geometrical parameters for stator and rotor.

Name	Expression	Value	Description
N_axmag	10	10	#Axial magnet segments
SCs_in_wire	20	20	Number of SCs in one wire
N_SC	200	200	Number of SC in one coil
w_SC	3 [mm]	0.003 m	Width of single SC
A_coil	h_coil*w_coil	4.8E-5 m²	Area for one layer
h_wire	h_HTS*SCs_in_wire	0.0016 m	Height of wire
N_wire	N_SC/SCs_in_wire	10	#Wires per coil.
h_coil	N_wire*h_wire	0.016 m	Wire height
w_wire	w_SC	0.003 m	
w_coil	w_SC	0.003 m	Wire width

Fig. 33. Geometrical parameters for the coils.

Name	Expression	Value	Description
Ec	1e-4[V/m]	1E-4 V/m	critical E-field
Ic	1478[A/cm]*w_HTS	443.4 A	critical current
Jc	Ic/(h_SC*w_HTS)	1.478E11 A/m²	(real) critical current density
Jc_eng	Jc*h_SC/h_HTS	1.8475E9 A/m²	eng. critical current density
N	25	25	Power in E-J
SC_load	0.2	0.2	fraction of Ic
I_peak	Ic*SC_load*SCs_in_wire	1773.6 A	peak phase current
J_c0	Ic/(w_SC*h_SC)	1.478E11 A/m²	
Jc_25K	3.717E11 [A/m^2]	3.717E11 A/m²	
Jc_30K	3.268E11 [A/m^2]	3.268E11 A/m²	
Jc_50K	1.97E11 [A/m^2]	1.97E11 A/m²	
Jc_60K	1.474E11 [A/m^2]	1.474E11 A/m²	
Jc_40K	2.543E11 [A/m^2]	2.543E11 A/m²	

Fig. 34. Electrical parameters for the HTS material.

Name	Expression	Value	Description
mu0	4*pi*1e-7[H/m]	1.2566E-6 H/m	permeability, air
mur_iron	2000	2000	rel. permeability, steel
murec_PM	1.1	1.1	recoil permeability PM
B_r	1.15[T]	1.15 T	Set to 1. Fourier coeffs dete...
f_mech	3500[rpm]	58.333 1/s	mechanical freq.
f_el	f_mech*p/2	233.33 1/s	electrical freq.
omega_el	2*pi*f_el[rad]	1466.1 rad/s	
t_max	1.9[ms]	0.0019 s	time for max torque
theta_q	2*pi*f_el*t_max [rad]	2.7855 rad	q axis angle
T_el	1/f_el	0.0042857 s	electrical period
Hsurf	ramp*B_r/(mu0*murec_PM)	0 A/m	
t	0[s]	0 s	time
rho_s	8120 [kg/m^3]	8120 kg/m³	steel density
rho_m	7500 [kg/m^3]	7500 kg/m³	magnet density
ramp	rm1(t)	0	
low1	eps	2.2204E-16	
PM_seg	45	45	# segments in PM
p_model	4	4	# poles in model
theta_seg	pi/PM_seg[rad]	0.069813 rad	angle per segment
theta_PM...	-(90-180/8)*2*pi/360[rad]	-1.1781 rad	must be set to hit q axis
omega_pm	omega_el	1466.1 rad/s	angular freq. of magnets.
phi_seg	1/180°*pi[rad]	0.017453 rad	PM segment angle

Fig. 35. Electrical and magnetic parameters.

Analytic
Plot   Create Plot

Label:	generate surface H-field (first boundary = 0)
Function name:	Hseg

▼ Definition

Expression:	Hsurf*(harmComp(a1, n1, seg_no)+harmComp(a2, n2, seg_no)+harmComp(a3, n3, seg_no))
Arguments:	seg_no, t
Derivatives:	Automatic

▷ Periodic Extension

▼ Units

Function: A/m

Argument	Unit
seg_no	1
t	s

Fig. 36. Function for generating the magnetic field in the segmented rotor.

Analytic
Plot   Create Plot

Label:	harmonic components
Function name:	harmComp

▼ Definition

Expression:	a_harm*sin(n_harm*omega_pm*(t)+n_harm*seg_no*theta_seg+n_harm*theta_seg/2+n_harm*theta_PM_offset)
Arguments:	a_harm, n_harm, seg_no
Derivatives:	Automatic

▷ Periodic Extension

▼ Units

Function: 1

Argument	Unit
a_harm	1
n_harm	1
seg_no	1

Fig. 37. Function for the harmonic components in the function.

Analytic
Plot   Create Plot

Label:	Kim model 60K
Function name:	Jc_of_B_60K

▼ Definition

Expression:	Jc_60K/((1+sqrt(eps+Jc_gamma_60_LF^(-2)*Bx^2+By^2)/Jc_B_0_60_LF)^Jc_alpha_60_LF)
Arguments:	Bx, By
Derivatives:	Automatic

▷ Periodic Extension

▼ Units

Function: A/m^2

Argument	Unit
Bx	T
By	T

Fig. 38. Function for the Kim-like model.

TABLE XII
AXIAL FLUX MACHINE DESIGN APPROACHES

Electric motor	Rotor speed (rpm)	Torque (kNm)	Power (kW)	Power density (kw/kg)	Efficiency	Design readiness	Application	SC implementation
Slotless Hallbach [3]	5000	—	≥ 250	12	95%	FEM software	Aircraft	None
Zhang [41]	9000	40	53.8	13	96%	Advanced	Aircraft	None
Bulk HTS [42]	3000	1.06	450	7.4	99%	Concept	Aircraft	Rotor
Bulk HTS [43]	5000	—	50	1	—	Advanced	Aircraft	Rotor
Single sided-SMC	25271	0.00126	0.834	2.38	77.5%	FEM software	—	None
SSSR	2000	0.0286	5.9	0.7632	94%	FEM software	High torque	None
SSDR	2000	0.0288	6.03	0.874	93.86%	FEM software	High torque	None
DSSR	2000	0.0297	6.2	0.92	94.2%	FEM software	High torque	None

TABLE XIII
SLOTLESS MACHINE DESIGN APPROACHES

Electric motor[1]	Rotor speed (rpm)	Power (kW)	Power density (kw/kg)	Phase voltage (V)	Efficiency	Technology readiness	Application	SC implementation
Generator [23]	3 000	10 000	24.7	6900	99,4%	Concept	Wind	Stator
IR-SPM [44]	7 000	10 000	23.4	1360	97.8%	Concept	Aircraft	Stator
Slotted-PMSM [4]	3550	2 500	14.7	434	—	FEM software	Aircraft	Stator
OR slotless [29]	18 000	10 000	14	–	97.7%	FEM software	–	Stator
GEN slotted [45]	35 000	5 000	8.8	670	98 %	Advanced	Aircraft	Rotor
IR HTS-wound [44]	7 000	10 000	64.8	1750	98.4%	Concept	–	Fully supercond.
OR HTS-bulk [44]	7000	10 000	104.6	1066	99.5%	Concept	Aircraft	Fully supercond.
Synchronous slotless [46]	3 000	10 000	25	6600	–	Advanced	Aircraft	Fully supercond.
DC Wound field [47]	6800	1 420	17.4	1200	98.9 %	Advanced	Aircraft	Fully supercond.
Shielded slotless	4500	2 500	≥ 25	750	99%	Concept	Aircraft	Fully supercond.
Generator slotless [48]	3000	10 000	13.7	–	—	Advanced	Marine	Fully supercond.

B. Tables and results from the specialization project.

Table XIII and XII showing the results from the topology study. Both for axial and radial machines.

Following section is copied directly from the specialization projects conclusion for the topology study.

Great efforts are being made in the field of electrical machines to replace the highly polluting jet fuel engine. Aiming at performance set by the Clean Aviation initiative, high-speed mega-watt scale motors [4]. SC implementation shows excellent promise for radial flux synchronous machines, where it can be the bridge to meeting the requirements made by the industry. Both slotless and slotted PM approaches, as well as HTS rotor configuration, are being researched. Where HTS bulk and HTS wound were seen. HTS in the rotor is more in the starting phase regarding TRL. It shows high potential but faces significant engineering challenges to be solved. The most promising of the typologies in the near future is the PMSM, where a slotless approach could be quite feasible, given its lighter design. The inner and outer rotor shows potential. Given more accessible cooling with an inner rotor approach, it is deemed more feasible for SC implementation. The axial flux machine comes with high torque and power density. However, the size of the discs is inherently limited by centrifugal forces. Few cases of axial flux machines met the power and speed requirements. Research with HTS in AFM is quite rare to be found as well. Therefore in this study, slotless typology with inner rotor is seen as superior to axial

flux machines for HTS aircraft applications.